

On the relation between magnetic field strength and gas density in the interstellar medium: A multiscale analysis

D. J. Whitworth,^{1,2,3*}  S. Srinivasan,¹ R.E. Pudritz,^{3,4} M.-M. Mac Low,⁵  G. Eadie,^{6,7,8} A. Palau,¹ J. D. Soler,⁹ R. J. Smith,¹⁰ K. Pattle,^{11,12} H. Robinson,⁴ R. Pillsworth,⁴ J. Wadsley,⁴ N. Brucy,^{3,13} U. Lebreuilly,¹⁴ P. Hennebelle,¹⁴ P. Girichidis,³ F. A. Gent,^{15,16,22}  J. Marin,² L. Sánchez Valido,^{5,17} V. Camacho,^{1,18} R. S. Klessen,^{3,19,20,21} and E. Vázquez-Semadeni¹

¹Universidad Nacional Autónoma de México, Instituto de Radioastronomía y Astrofísica, Antigua Carretera a Pátzcuaro 8701, Ex-Hda. San José de la Huerta, 58089 Morelia, Michoacán, México

²Jodrell Bank Centre for Astrophysics, Dept. of Physics and Astronomy, University of Manchester, Oxford Road, Manchester M13 9PL, UK

³Universität Heidelberg, Zentrum für Astronomie, Institut für Theoretische Astrophysik, Albert-Ueberle-Str. 2, 69120 Heidelberg, Germany

⁴Department of Physics and Astronomy, McMaster University, 1280 Main Street West, Hamilton, ON, L8S4K1, Canada

⁵Department of Astrophysics, American Museum of Natural History, 200 Central Park West, New York, NY 10024, USA

⁶David A. Dunlap Department of Astronomy & Astrophysics, University of Toronto, 50 St George St, Toronto, ON, M5S 3H4, Canada

⁷Department of Statistical Sciences, University of Toronto, 700 University Avenue, Toronto, ON M5G 1Z5, Canada

⁸Data Sciences Institute, University of Toronto, 700 University Avenue, Toronto, ON, M5G 1Z5, Canada

⁹Istituto di Astrofisica e Planetologia Spaziali (IAPS). INAF. Via Fosso del Cavaliere 100, 00133 Roma, Italy

¹⁰SUPA, School of Physics and Astronomy, University of St Andrews, North Haugh, St Andrews, KY16 9SS, UK

¹¹Department of Physics and Astronomy, University College London, Gower Street, London WC1E 6BT, United Kingdom

¹²Centre for Astronomy, School of Natural Sciences, University of Galway, University Road, Galway H91 TK33, Ireland

¹³Centre de Recherche Astrophysique de Lyon UMR5574, ENS de Lyon, Univ. Lyon1, CNRS, Université de Lyon, 69007, Lyon, France

¹⁴Université Paris-Saclay, Université Paris Cité, CEA, CNRS, AIM, 91191, Gif-sur-Yvette, France

¹⁵HPCLab, Department of Computer Science, Aalto University, PO Box 15400, FI-00076, Espoo, Finland

¹⁶Nordita, KTH Royal Institute of Technology and Stockholm University, Hannes Alfvéns väg 12, Stockholm, SE-106, Sweden

¹⁷Department of Physics & Astronomy, Barnard College, Altschul Hall 504A, 3009 Broadway, New York, NY 10027, USA

¹⁸Center of Astronomy and Gravitation, Department of Earth Sciences, National Taiwan Normal University, 88, Sec. 4, Ting-Chou Rd., Wenshan District, Taipei 116, Taiwan R.O.C

¹⁹Universität Heidelberg, Interdisziplinäres Zentrum für Wissenschaftliches Rechnen, Im Neuenheimer Feld 225, 69120 Heidelberg, Germany

²⁰Harvard-Smithsonian Center for Astrophysics, 60 Garden Street, Cambridge, MA 02138, USA

²¹Fellow at the Radcliffe Institute for Advanced Studies at Harvard University, 10 Garden Street, Cambridge, MA 02138, USA

²²School of Mathematics, Statistics & Physics, Newcastle University, Newcastle upon Tyne NE1 7RU, UK

Accepted XXX. Received YYY; in original form ZZZ

ABSTRACT

The magnetic field strength to gas density relation in the interstellar medium is of fundamental importance. We present and compare Bayesian analyses of the B - n relation for two comprehensive observational data sets: a Zeeman data set and 700 observations using the Davis-Chandrasekhar-Fermi (DCF) method. Using a hierarchical Bayesian analysis we present a general, multi-scale broken power-law relation, $B = B_0(n/n_0)^\alpha$, with $\alpha = \alpha_1$ for $n < n_0$ and α_2 for $n > n_0$, and with B_0 the field strength at n_0 . For the Zeeman data we find: $\alpha_1 = 0.15^{+0.06}_{-0.09}$ for diffuse gas and $\alpha_2 = 0.53^{+0.09}_{-0.07}$ for dense gas with $n_0 = 4.00^{+12.7}_{-2.90} \times 10^3 \text{ cm}^{-3}$. For the DCF data we find: $\alpha_1 = 0.26^{+0.15}_{-0.15}$ and $\alpha_2 = 0.77^{+0.14}_{-0.15}$, with $n_0 = 13.9^{+10.1}_{-7.30} \times 10^4 \text{ cm}^{-3}$, where the uncertainties give 68% credible intervals. We perform a similar analysis on nineteen numerical magnetohydrodynamic simulations covering a wide range of physical conditions from protostellar disks to dwarf and Milky Way-like galaxies, completed with the AREPO, FLASH, PENCIL, and RAMSES codes. The resulting exponents depend on several physical factors such as dynamo effects and their time scales, turbulence, and initial seed field strength. We find that the dwarf and Milky Way-like galaxy simulations produce results closest to the observations.

Key words: ISM: magnetic fields – Magnetohydrodynamics (MHD)

* E-mail: d.whitworth@irya.unam.mx

1 INTRODUCTION

The importance of magnetic fields in the interstellar medium (ISM) has been debated ever since their discovery more than 70 years ago (Davis 1951). Since then, magnetic fields have been found in a wide variety of astrophysical systems including galaxy clusters (e.g. Carilli & Taylor 2002), spiral galaxies (e.g. Beck 2015), the diffuse interstellar medium (ISM), giant molecular clouds (e.g. Crutcher 2012), regions of star-cluster formation (e.g. Pudritz et al. 2014; Kirk et al. 2015), and protostellar discs (e.g. Hull & Zhang 2019). It is well-recognised that magnetic fields may play a significant role in gas dynamics across many decades of physical scale which have very different properties. As an example, the question of their connection to the ISM and whether they support giant molecular clouds against collapse and affect star formation drives major observational programs (e.g. Crutcher et al. 2010, hereafter C10; Pillai et al. 2015; Planck Collaboration et al. 2016; Soler 2019) and numerical simulations (e.g. Girichidis et al. 2018; Gent et al. 2021; Ibáñez-Mejía et al. 2022; Robinson & Wadsley 2023, Whitworth et al. 2023, hereafter W23; Zhao et al. 2024) of ever growing sophistication and resolution.

Mestel (1966) first proposed a theoretical connection between magnetic field strength and density in studies of the idealised collapse of dense, magnetized, gravitationally bound spheres of gas. He found two possible power-law relationships of the form $B \propto n^\alpha$, depending on the strength of the field. In the case of weak fields, the morphology of the cloud is not affected, so the field is dragged in a spherical or isotropic collapse, resulting in $|\mathbf{B}| \propto n^{2/3}$. However, stronger fields constrain the gas, which then collapses parallel to field lines, giving rise to a $|\mathbf{B}| \propto n^{1/2}$ scaling.

The B - n relation is far more general and plays an important role in a much larger set of astrophysical environments. While Mestel (1966) derived a relation for self-gravitating systems without turbulence, non-self gravitating turbulent environments can also lead to a similar relation (Molina et al. 2012). As an example of the effects that turbulence can have, Passot & Vázquez-Semadeni (2003) showed that in turbulent magnetohydrodynamics (MHD) simulations without self-gravity, the relationship between magnetic pressure, B^2 , and density depends on the type of MHD wave mode predominantly active in the flow; the fast mode produces a scaling $B^2 \propto n^2$, while the slow mode produces a scaling $B^2 \propto c_1 - c_2 n$, where c_1 and c_2 are constants. More generally, turbulence drives dynamo action that establishes field strengths in media of widely different densities, from the diffuse ISM, to the denser portion of molecular clouds. Thus Gent et al. (2021) showed that the small-scale dynamo (SSD) is driven to saturation in a turbulent multiphase diffuse medium. It is therefore important to encompass a broad range of dynamical simulations and physical processes, and to compare the B - n relations produced with the most comprehensive observational data sets available.

In a seminal paper, C10 compiled Zeeman measurements of line-of-sight magnetic field strengths from a variety of published observational data sets. Low density gas measurements were acquired from HI and OH lines, whereas higher gas densities used OH and CN lines. Their Bayesian analysis of Zeeman measurements of 137 molecular clouds yielded a power-law relation of $B \propto n^{2/3}$ above densities of $n = 300 \text{ cm}^{-3}$,

while below this density the magnetic field strength was interpreted as being independent of gas density, i.e. $B \propto n^0$.

C10 interpreted the high density power-law exponent as evidence that magnetic energy does not dominate over gravity at intermediate to high densities. This has been supported by some subsequent observations (Soler 2019) and simulations (Seifried et al. 2020; Ibáñez-Mejía et al. 2022; Whitworth et al. 2023). Other work gives different results. For example Tritsis et al. (2015) re-analysed the Zeeman data used by Crutcher, and showed that with relaxed assumptions on the errors a smaller index is found, with $B \propto n^{1/2}$ being more likely. On the other hand, Jiang et al. (2020) found a higher value for the exponent; $\alpha \sim 0.72$, and argue that due to the observational uncertainties in both B and n it is difficult to accurately determine the exponent and density at which the turn over occurs.

An important recent development is that observational data sets have been greatly expanded with submillimeter polarization measurements in denser regions using instruments like ALMA or the Submillimeter Array (SMA; Pattle et al. 2022). Observations of polarized thermal dust emission and density, along with the velocity dispersion σ_v provide estimates of the plane-of-sky magnetic field strength. Using a combination of the scatter of polarization directions and the strength of turbulence implied by the velocity dispersion, the local field strength in the gas can be estimated by the Davis-Chandrasekhar-Fermi (DCF) method (Davis 1951; Chandrasekhar & Fermi 1953).

The main assumptions of the DCF method are: 1) that there is an underlying uniform magnetic field perturbed by the turbulent gas motions, 2) that the dispersion in polarization position angles, σ_{PA} , is produced by the propagation of incompressible MHD waves (i.e., Alfvén waves), and 3) that the gas kinetic energy (which is assumed to be fully turbulent) is completely transferred to magnetic energy fluctuations. The DCF method allows the determination of the plane-of-sky component of the magnetic field strength,

$$B_{\text{pos}} = f(4\pi\rho)^{1/2} \frac{\sigma_v}{\sigma_{PA}}, \quad (1)$$

where the gas mass density is ρ and f is a correction factor further discussed below.

One source of uncertainty in the DCF method is that whereas it has been generally assumed that σ_{PA} is produced by the propagation of incompressible MHD waves, compressible modes of turbulence could also make a significant contribution. Skalidis & Tassis (2021, henceforth ST) and Skalidis et al. (2021) develop a new method to take the compressible modes into account. This method is new and has yet to be rigorously tested observationally and numerically but the early results are promising.

Other recent theoretical magneto-gravo-turbulent simulations (Mocz et al. 2017; Auddy et al. 2022) find that the power-law exponent for diffuse gas in isolated molecular clouds increases as the Alfvénic Mach number increases. Models of individual, isolated, collapsing cores by Cao & Li (2023) show how their B - n relationship evolves. At the end of the simulations the cores match the Crutcher result, suggesting that it is driven by the gas being magnetically super-critical with super Alfvénic turbulence (Li et al. 2013; Myers & Basu 2021).

The large body of numerical work now available is trans-

forming our understanding of the B - n relation. On the scale of dwarf galaxies W23 reported a relationship of $|\mathbf{B}| \propto n^{1/2}$ in high resolution simulations. Other theoretical work also shows a similar exponent (Hennebelle et al. 2008; Banerjee et al. 2009; Girma & Teyssier 2023). However, in different simulations the B - n relation can vary depending on numerous conditions such as initial seed field strength (Robinson & Wadsley 2023), dynamo effects (Gent et al. 2024; Korpi-Lagg et al. 2024), embedded ISM dynamics (Ibáñez-Mejía et al. 2022), and time dependencies (Robinson & Wadsley 2023; Konstantinou et al. 2024). These can all affect whether a break in the relation appears at some density and the value of the exponents.

We here compare extended observational data sets with the results of simulations, performed by our team using a variety of MHD codes, of a wide variety of regions in the ISM, from protostellar discs to entire galaxies. In general, these simulations show that up to densities of 10^5 cm^{-3} , ideal MHD applies: the field is tied to the flow of the gas as the effects of ambipolar diffusion are subdominant (e.g. Mac Low & Klessen 2004). For galaxy scale simulations ideal MHD is sufficient as they do not resolve down to scales where these effects become important. Simulations that model protostellar discs (Lebreuilly et al. 2021) and individual star formation (Moscadelli et al. 2022) include non-ideal MHD physics at densities where ambipolar diffusion becomes important.

The goal of this paper is to address two basic questions. What is the general density-magnetic field relation across a wide range of ISM densities? What are the physical processes driving it? We present a new multi-scale, hierarchical Bayesian analysis of this relationship for an extended set of Zeeman and DCF observations, as well as a non-hierarchical Bayesian analysis for a large number of current numerical simulations.

Section 2 briefly describes the methods used in our analysis; Section 3 shows the results from recent observations; Section 4 shows the results from simulations using different initial conditions and codes; Section 5 discusses the results and compares the observational results to the numerical results; and Section 6 summarises our findings.

2 METHODS

In this section we briefly describe our methods, leaving many of the details to a series of Appendices. We first introduce the functional form we assume for the B - n relation (Sect. 2.1) and describe our Bayesian analysis in Section 2.2; Appendix A provides a more detailed description of the analysis and error treatment. We then outline the observational and numerical data sets used in this study, along with their uncertainties in Sections 2.3 and 2.4.

2.1 Functional Form

In order to compare and contrast with the original C10 relation, we assume a two-part broken power-law B - n relation for our model, similar to theirs;

$$|\mathbf{B}| = B_0 \begin{cases} (n/n_0)^{\alpha_1} & \text{if } n \leq n_0, \\ (n/n_0)^{\alpha_2} & \text{if } n > n_0. \end{cases} \quad (2)$$

where α_1 and α_2 are the exponents of the two power-laws, n_0 is the number density of the break in the power-law, and B_0 is the magnetic field strength at the break. Our model differs from C10 in that α_1 is not set to zero. We do not consider a maximum on B but use the reported values in their respective publications. We discard the flexibility function free parameter that was used in C10 which denotes the trust in the probability density function (PDF) used in the prior. As described in the following section, we also consider a more detailed hierarchical Bayesian approach.

One concern in using the DCF as a complementary method to Zeeman measurements is in calibrating the accuracy of the polarization maps. Heitsch et al. (2001) did this by performing synthetic dust polarisation observations (DCF-like observations) on the data produced by simulations of three-dimensional MHD turbulence driven for self-gravitating molecular clouds. They showed that the synthetic observations produce an increase in field strength by a factor of a few similar to what the DCF method is expected to produce in gravitationally dominated regions, so they argued that the DCF method is applicable. Chen et al. (2022) also model synthetic DCF observations as well as structure function-DCF observations, noting that this is a preferred method. Again, their synthetic results are similar to those from observations, but uncertainties in the linewidth may be more important than errors in polarization. Based on these results, the DCF method is a valid approach for our purposes as long as we are aware of its limitations and take them into account.

Including DCF observations has two advantages: the larger data sets available enable stronger statistical analyses, and the data covers a larger density range, up to $n \simeq 10^9 \text{ cm}^{-3}$. Pattle et al. (2022) note that at densities of $n > 10^7 \text{ cm}^{-3}$ the field strength appears to become constant, as we show in Appendix A7. However, we refrain from using a three-value power-law primarily because above this density, the DCF method becomes unreliable for various reasons. For example, in this regime it is expected that dust grains will align more to the radiation field than to the magnetic field (Lazarian 2020).

2.2 Bayesian Analysis

In this work, we perform Bayesian inference on three different data sets: two observational, and one based on our large set of simulations. For the observational data, we use a hierarchical Bayesian model¹ and for the simulations, we use a non-hierarchical Bayesian model.

The details of the hierarchical Bayesian model for the observation data are given in Appendix A2. The hierarchical Bayesian model allows us to:

- (i) model the measurements of n and B as draws from a distribution centred on their true but unknown values,
- (ii) carefully and coherently account for the measurement uncertainties in n and B ,
- (iii) comprehensively study the covariance in measurement uncertainties inherent to the DCF data set, and

¹ Initially, we tried a non-hierarchical model for the observational data. However, we found that excluding the information about the covariance structure in n and B measurements led to bimodal posterior distributions (see Appendix A1.1).

(iv) introduce physically motivated but not too-constrained priors on the model parameters.

In Section 2.3, we give an overview of how the uncertainties are incorporated into the hierarchical Bayesian model. In all forms of Bayesian analysis, the choice of the prior is important and can heavily influence the results. Appendix A2 provides a more detailed description of the likelihood, priors, and hyperpriors.

One point that has been raised in the literature (Tritsis et al. 2015; Jiang et al. 2020) is the value C10 chose for the error of n_0 . In the original survey data no errors were reported and so a relative uncertainty of a factor of two was chosen. In Appendix A4 we test three different values for the relative uncertainty, 2, 5, and 9. These are based on the original choice, the best result from Jiang et al. (2020) of nine, and an intermediate value. We find there is some variation in the results when we change the uncertainty, but it is not statistically significant in our analyses, so we choose a factor of 5 (see Appendix A4 for a detailed discussion).

Our comparison data set is the ensemble of all of our numerical simulations. Here we employ a broad uniform PDF of priors for all parameters due to the large range of densities covered in the simulations, $10^{-5} < n_0 < 10^{13} \text{ cm}^{-3}$ and the resulting spread of data in each. Due to the amount of data in each simulation—over 10^6 data points in each model—we use a non-hierarchical Bayesian model for computational efficiency. We perform inference on five random samples of 10^5 data points from each simulation and combine the results to compute credible intervals² for the parameters. A detailed discussion of the non-hierarchical model used can be found in Appendix A3.

2.3 DCF errors

When B_{pos} is inferred from the DCF method, the main uncertainties come from the following sources:

(i) Density: The estimate of the density in Eq. (1) is usually obtained by combining a mass estimate derived from thermal dust emission with the assumption of a specific geometry. To estimate the mass, a specific dust temperature and a dust opacity at the observing frequency are usually assumed (e.g., Könyves et al. 2015; Elia et al. 2017). These two quantities are highly uncertain, with the dust opacity varying by a factor of 2–4 (e.g., Ossenkopf & Henning 1994; Li et al. 2024).

(ii) Velocity dispersion: The velocity dispersion is measured from a molecular gas tracer. It is typically assumed that the entire velocity dispersion, which is usually dominated by non-thermal motions, is due to turbulence only. Therefore, the uncertainty comes from the specific properties of the tracer used, and from the fact that a non-negligible part of the velocity dispersion might be due to bulk, non-turbulent, motions. If this is not taken into account, the mag-

² We compute two types of 68% credible intervals: equal-tailed intervals which reject 16% of the total probability on either side of the median, and highest posterior density (HPD) intervals that select the narrowest interval containing 68% of the total probability. For unimodal distributions, HPD intervals will contain the mode of the distribution.

netic field can be overestimated by a factor of 2, as shown in Palau et al. (2021).

(iii) Polarization position angle dispersion: When a number of polarization segments have been detected in a specific region, σ_{PA} can be characterized with different measures, such as the standard deviation of the position angles, the width of a Gaussian fit to the position angle histograms, or more sophisticated values based on the structure function as proposed by Hildebrand et al. (2009) or Houde et al. (2009). Even if the structure functions account for the mean-field orientation, they can be strongly affected by the sampling in the polarization data (e.g., Soler et al. 2016, see below). These different approaches to estimate σ_{PA} typically differ by a factor of two (e.g., Palau et al. 2021).

(iv) f factor: The correction factor f has been proposed to correct for several biases, such as projection effects along the line-of-sight, the averaging of the magnetic field within the beam, the use of only one of the three velocity components, and the lack of exact equipartition between the magnetic energy of the perturbed magnetic field and the kinetic energy. This factor has been estimated from numerical simulations to usually be 0.5, although it can reach lower values of around 0.2 (e.g., Heitsch et al. 2001; Ostriker et al. 2001; Liu et al. 2022a).

(v) Sparse sampling effects: Due to sensitivity limitations, only a fraction of the total area emitting polarized radiation is detected, restricting the reliability of the measurement. An extreme case is when very few polarization segments are detected, suggesting a relatively uniform and strong field, while deeper observations reveal an underlying more turbulent field. The relative uncertainty due to sparse sampling can reach up to 60% (Palau et al. 2021). This uncertainty is explained in detail in Liu et al. (2019).

(vi) Cloud extent along the line of sight (LOS): Usually, there is limited information on the target’s size in the LOS direction. This uncertainty can lead to considerable error in the density estimations. For example, Angarita et al. (2024) show that clouds could be up to ten times deeper than predicted through plane-of-sky observations.

In addition to the aforementioned uncertainties, the choice of the DCF or the ST method for interpretation of the polarization data can introduce additional biases. The main difference between the DCF and ST methods is the dependence on σ_{PA} (apart from the $\sqrt{2}$ factor): in the DCF method, $B_{\text{pos}} \propto 1/\sigma_{\text{PA}}$, while in the ST method, $B_{\text{pos}} \propto 1/\sqrt{\sigma_{\text{PA}}}$. Since in most cases $\sigma_{\text{PA}} < 1 \text{ rad}$, the ST method results in B_{pos} systematically smaller by a factor of 2–4 compared to the values obtained with the DCF method.

Taking into account the combination of all the potential uncertainties associated with the B_{pos} measurements, the global uncertainties could reach an order of magnitude. Further details on the uncertainties associated with magnetic field measurements can be found in the recent reviews by Liu et al. (2021), Liu et al. (2022a, see their Sec. 2.2), and Pattle et al. (2022).

2.4 Observational data sets

The Zeeman splitting data of C10 (their Table 1), used for their analysis, provides estimates of the line-of-sight compo-

ment of the magnetic field. For the DCF data in this work, we used the compilation of [Pattle et al. \(2022\)](#).

The data is split into two different sets in order to provide a statistical analysis consisting of the original Zeeman data along with a new data set based on the DCF measurements from [Pattle et al. \(2022\)](#). These are:

- 1 Zeeman: The Zeeman data from [C10](#).
- 2 DCF: The DCF data from [Pattle et al. \(2022\)](#) with only symmetric errors in both n and B .

In addition to the two main data sets we tested different subsets of the data. First we tested whether unrealistically small error estimates were biasing the results. To do this we set any error that is smaller than 15% to 15%, and the same for 50%. We saw no statistically significant change in the results, and so do not include this analysis. We also tested whether an outlier in the DCF data set was biasing our results (see Appendix A7). We test the scaling ratio of [Pattle et al. \(2022\)](#) between DCF data and Zeeman data in Appendix A5 but due to inherent uncertainties in this we do not consider this a main result. Finally, we also looked at the full data set from [Pattle et al. \(2022\)](#) with the known errors plus errors computed using a kernel density estimate (KDE) for the data that was lacking reported errors (see Appendix A4.3 for a discussion on the errors). We report these results in Appendix A7, as we consider them less reliable due to the inherent uncertainty in the KDE error estimates.

2.5 Numerical simulations: methods and data sets

We perform the non-hierarchical Bayesian analysis on nineteen numerical simulations that cover a wide range of initial conditions, densities, magnetic field strengths, and scales. The systems covered in our simulations range from full Milky Way-like galaxies to protoplanetary discs.

The simulations themselves were executed with the codes AREPO ([Springel 2010](#)), FLASH ([Fryxell et al. 2000](#)), RAMSES ([Teyssier 2002](#)), and PENCIL ([Brandenburg & Dobler 2002; Brandenburg et al. 2020](#)). These codes use different types of meshes and refinement criteria. AREPO solves the MHD equations on a quasi-Lagrangian Voronoi moving mesh that provides high spatial resolution in high-density regions. FLASH and RAMSES are adaptive mesh refinement (AMR) codes that use hierarchical nested Cartesian grids to achieve high resolution in regions of interest. PENCIL is a high-order, uniform grid code using sixth-order space and fourth-order time derivatives. We refer the reader to the cited method papers for a more detailed description of each code.

For each simulation presented here, we refer to the original publication for a detailed discussion of their numerical setup. The high-resolution simulations of dwarf galaxies presented here are novel and have been run specifically for this work, so we summarize the key differences to the original simulations in Appendix B.

For each simulation, we compare the distribution of $|\mathbf{B}|$ against the number density n in each computational cell to the original relation of [C10](#). The volume-weighted average fit to the data is calculated by binning the data into 500 equally sized log-spaced density bins and then calculating the volume-weighted average of each bin.

We volume-weight the magnetic field in the uniform grid code as this is most comparable to the Eulerian nature of the

code. For the AREPO and AMR simulations, we volume weight due to oversampling in the densest regions. The meshes are non-uniform and so a grid average would be biased towards the densest regions. By volume weighting, we take an Eulerian point of view, meaning that we get the typical view at a randomly chosen point in space.

3 OBSERVATIONAL RESULTS

Figure 1 displays the joint distribution of the posterior samples from our hierarchical Bayesian analysis of the observational data. Both the joint and marginal parameter distributions for the Zeeman data (left) and DCF data (right) are shown. The distributions show some strong correlations between parameters, which is expected. For example, the relationship between n_0 and B_0 and the relationship between α_1 and B_0 are particularly strong.

Using the samples from the posterior distributions in Figure 1, the inferred relationships between B and n are illustrated in Figure 2. It shows two generalised forms of the relationship, one based on the Zeeman data from [C10](#) and the other based on the DCF data from [Pattle et al. \(2022\)](#). The first of these compares the data with the inferred maximum a posteriori (MAP) model constructed using posterior samples for the Zeeman data. The second compares the DCF data set both with the MAP model and with the range of posterior predictions for this data set, demonstrating that the models can reproduce the range of observed values.

Before going further, we want to stress a key difference between the bottom two panels in Figure 2, because this is important for interpretation. If one wishes to read the mode of the posterior as the most likely values of $(\alpha_1, \alpha_2, n_0, B_0)$, then one should look at the left-hand panel. The red line corresponds to the unique set of parameter values $(\alpha_1, \alpha_2, n_0, B_0)$ at the MAP. This is a *point estimate* of the posterior mode derived from our samples from the posterior distribution; this line does not correspond to any particular draw from the posterior.

A more Bayesian perspective is presented in the right-hand panel, which shows the pointwise predicted relationship of magnetic field to number density, as predicted by the posterior distribution. The blue region is the 68% Bayesian credible region, which encompasses our uncertainty in the prediction given the data, our priors, and the assumed model. The pointwise predicted relationship is calculated as follows:

1 At each value of n , the value of B is calculated for every sample $(\alpha_1, \alpha_2, n_0, B_0)$ from the posterior distribution. Because we have $5000 \times 4 = 20000$ samples from the posterior, this results in 20 000 values of B .

2 For each n , the median of the B values is calculated and plotted in purple, resulting in the relationship shown.

3 For each n , the 20 000 values of B from step 1 are used to compute 16th and 84th percentiles to construct the 68% equal-tailed interval, shown in blue.

Table 1 summarises the estimated median and mode along with the corresponding 68% credible intervals for each parameter, calculated from the posterior samples. The exponent in the low-density regime, α_1 , is tightly constrained and positive in all cases. Moreover, its value depends on the data set. Likewise, the corresponding field strength normalisation B_0 is

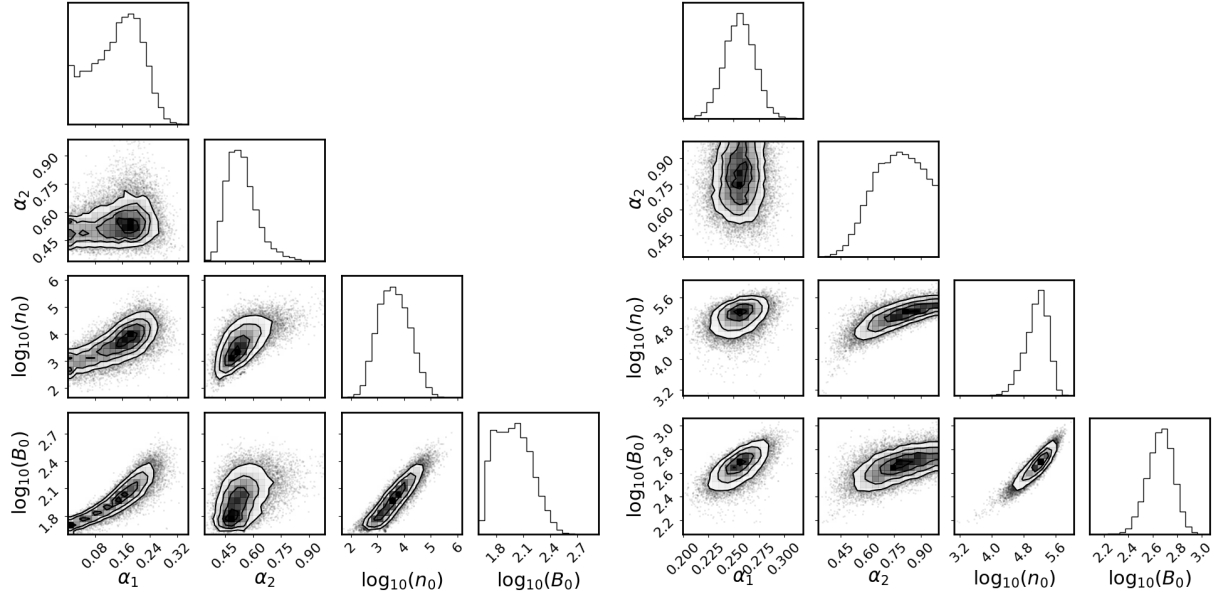


Figure 1. The joint and marginal parameter distributions produced by the hierarchical Bayesian model for the Zeeman (left) and DCF (right) data sets. Almost all joint distributions show a significant correlation between the parameters.

uncertain, and varies between datasets. This is not surprising because there is a strong correlation or degeneracy between B_0 and n_0 (Fig. 1). We discuss this further in Section 5.2.

In our analysis, we note that we have excluded one data point in the DCF data that lies far beyond $n = 10^7 \text{ cm}^{-3}$. We conducted our analysis with and without this data point and found that it was highly influential (see Appendix A7). This influential data point also leads us to explore the influence of including many high-density values. In Appendix A7, we perform an analysis on the complete DCF data set and find that the results become unphysical with the high-density values included.

Figure 3 shows the median and MAP parameter estimates of the posterior samples and the corresponding 68% credible intervals for the two observational data sets as well as each of the nineteen numerical simulations examined in this work. The medians are estimated from the combined posterior samples from each data set with errors propagated through. The data without visible error bars around the median and MAP have narrow, but non-zero, credible errors.

The Zeeman and DCF data agree in having $\alpha_1 > 0$ in the diffuse gas, $\alpha_2 > 0.5$ in the dense gas, a break density $n_0 > 10^3 \text{ cm}^{-3}$, and $B_0 > 50 \mu\text{G}$. These are useful points of comparison to the models, despite the remaining substantial variation in the values for each estimate of the B - n relationship.

4 NUMERICAL SIMULATION RESULTS

In this section, we use a non-hierarchical Bayesian approach to deduce the B - n relations from a heterogeneous set of numerical simulations using the different codes, scales, and approximations described in Section 2.5. Table 2 lists the codes used, systems simulated, resolution, density range covered, and whether self-gravity is turned on. Because the numerical simulations span a much larger range of n than the observa-

Data set	α_1	α_2	n_0 (10^4 cm^{-3})	B_0 (μG)
Zeeman				
Median	$0.15^{+0.06}_{-0.09}$	$0.53^{+0.09}_{-0.07}$	$0.40^{+1.3}_{-0.30}$	95^{+60}_{-36}
MAP	$0.18^{+0.05}_{-0.10}$	$0.50^{+0.10}_{-0.10}$	$0.26^{+0.53}_{-0.25}$	61^{+63}_{-14}
DCF				
Median	$0.26^{+0.01}_{-0.01}$	$0.77^{+0.14}_{-0.15}$	14^{+10}_{-7}	460^{+120}_{-100}
MAP	$0.26^{+0.01}_{-0.02}$	$0.78^{+0.15}_{-0.14}$	12^{+8}_{-8}	440^{+130}_{-93}

Table 1. Median parameter estimates for the observational B - n relation with 68% equal-tailed intervals calculated from the posterior samples, along with the MAP value and the corresponding 68% highest posterior density (HPD) intervals. Both data sets have a tightly constrained, positive median α_1 and higher n_0 than that reported in C10 in both the median and MAP results.

tional data, as well as being much larger data sets, we use the non-hierarchical Bayesian approach with uniform priors described in Appendix A3.

Figure 3 shows the parameters derived for each simulation, and Appendix A8 presents these same data in tabular form. We provide a detailed description of each simulation in the following subsections.

Examining the results, we find large variations in all free parameters across the simulations, for example, by a factor of over 10^4 in n_0 . Although no simulation completely matches the observational result, we find that the galactic scale simulations are most similar, with MHD_SAT_HR being the closest match for the exponents. However, only one simulation has values of both n_0 and B_0 that lie within 1σ of the original relationship, MHD_10. The exponent of the diffuse gas for each simulation, α_1 , varies from -0.27 in IMHD to 0.84 in MHD_10_LR. Most simulations that trace the dense gas well show an α_2 of ~ 0.5 or higher. The exceptions are the simulations run for shorter time scales like B3, B6,

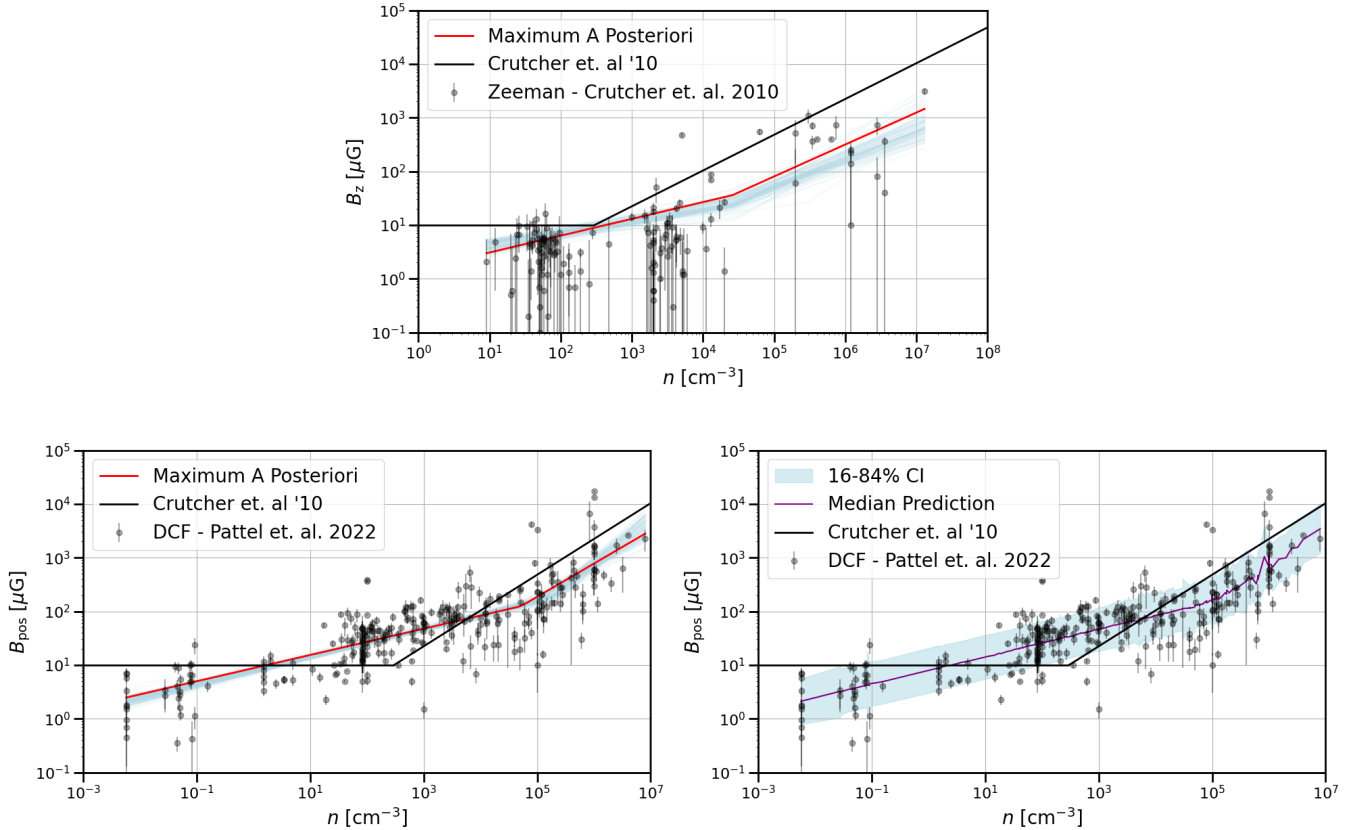


Figure 2. The inferred relationship of magnetic field strength as a function of number density, based on a Bayesian analysis of the observations. The *solid black line* in all plots is the relationship proposed by C10. *Top Panel:* The inferred MAP relationship between B_z and n based on our hierarchical Bayesian analysis applied to the Zeeman data (red line) from C10, along with the relationship predicted by 100 random samples from the posterior (blue lines). *Bottom Panels:* The inferred $B_{\text{pos}}-n$ relationship, based on our hierarchical Bayesian analysis applied to the DCF data set from Pattle et al. (2022). The bottom left panel shows the MAP relationship from the posterior (red line) and 100 random samples from the posterior (blue lines). The bottom right panel shows the posterior predictive plot: the median pointwise

predicted field for each density value in the DCF data (purple line) and the 68% credible interval around this median (blue region), which reproduces the range of observations (circles with error bars). A description of the method for producing the pointwise predictive plot is given in the text.

KPC_LOW, KPC_HIGH, and the dynamo models of Gent et al. (2021) and Gent et al. (2024), which do not reach sufficiently high densities. We discuss the details of these different simulations in the following subsections.

4.1 Core collapse simulations

Figure 4 presents data from simulations of molecular cloud cores collapsing to form protoplanetary discs and envelopes, computed with the AMR code RAMSES in either the ideal MHD limit or including non-ideal ambipolar diffusion (Lebreuilly et al. 2021). The resolution of these simulations goes from 0.0120 pc (2460 au) in the most diffuse gas to 5.84×10^{-6} pc (1.2 au) in the densest gas. A uniform seed field of $\sim 9.4 \times 10^{-5}$ G is initialised in the core. For more detail we refer to the original publication. This simulation includes higher density gas characteristic of protostellar discs than is possible to measure in the observed systems. There appears to be a well-defined B - n relation with a best-fitting power-law index of $\alpha_2 \sim 0.56$. The diffuse gas index α_1 has a negative value as the simulations only include small amounts

of lower-density gas in outflow cavities unrepresentative of the ISM. We see that the fits to the two simulations are similar. This suggests that at the densities modelled, ambipolar diffusion has not strongly decoupled the ions and the field from the bulk of the gas. The drop in the power law towards a plateau in the NI model at the very highest densities may represent the first indication of substantial decoupling at high densities ($n > 10^9$ cm $^{-3}$). This decoupling behaviour is well documented (Masson et al. 2016; Vaytet et al. 2018; Hennebelle et al. 2020; Commerçon et al. 2022).

4.2 Stratified box simulations

We here present results from stratified, horizontally periodic domains with and without galactic shear. Each simulation includes supernova (SN) driving and a disc gravitational potential. All simulations except those of Gent et al. (2021) and Gent et al. (2024) include self-gravity. For a more detailed discussion of the initial conditions of each simulation, we point the reader to the original publications.

The results from two (0.5 kpc) 3 stratified box simulations

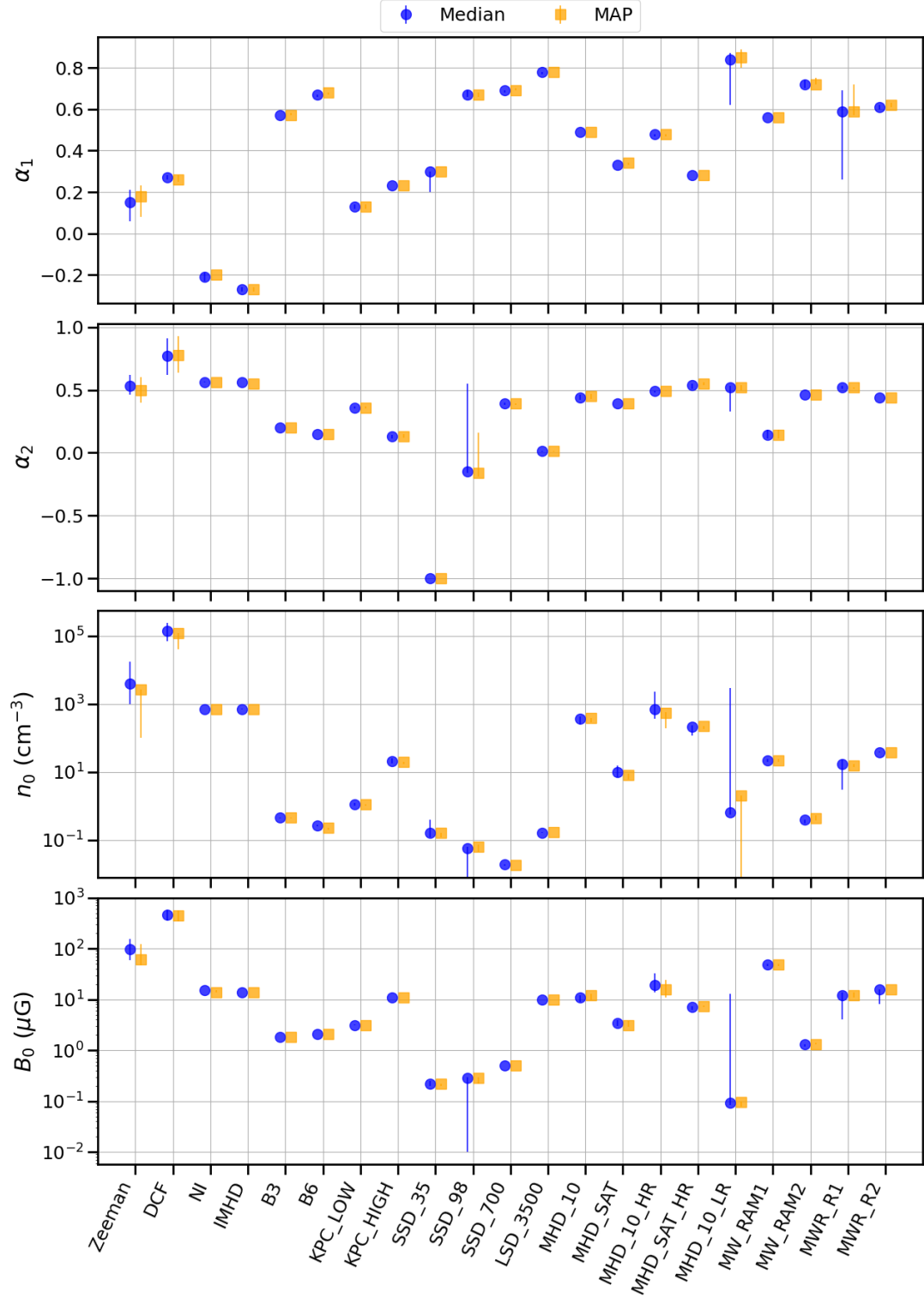


Figure 3. MAP (orange squares) and median (blue circles) parameter estimates for the two observational data sets and all nineteen numerical simulations. Error bars give the 68% credible intervals where they are larger than the symbol size. A tabulation of these data is available in Appendix A8.

Simulation	Code	System	Min Δx (pc)	Density range (cm^{-3})	Self-gravity	Reference
NI	RAMSES	Core Collapse	5.84×10^{-6}	10^1 – 10^{13}	Yes	Lebreuilly et al. (2021)
IMHD	RAMSES	Core Collapse	5.84×10^{-6}	10^1 – 10^{13}	Yes	Lebreuilly et al. (2021)
B3	FLASH	Stratified Box	1	10^{-6} – 10^5	Yes	Girichidis et al. (2018)
B6	FLASH	Stratified Box	1	10^{-6} – 10^5	Yes	Girichidis et al. (2018)
KPC_LOW	RAMSES	Stratified Box	4	10^{-4} – 10^4	Yes	Brucy et al. (2023)
KPC_HIGH	RAMSES	Stratified Box	0.12	10^{-4} – 10^4	Yes	Colman et al. (2022)
SSD_35	PENCIL	Stratified Box + Shear	1	10^{-4} – 10^2	No	Gent et al. (2021)
SSD_98	PENCIL	Stratified Box + Shear	1	10^{-4} – 10^2	No	Gent et al. (2021)
SSD_700	PENCIL	Stratified Box + Shear	1	10^{-4} – 10^2	No	Gent et al. (2021)
LSD_3500	PENCIL	Stratified Box + Shear	4	10^{-4} – 10^0	No	Gent et al. (2024)
MHD_10	AREPO	Dwarf Galaxy	0.1	10^{-4} – 10^5	Yes	W23
MHD_SAT	AREPO	Dwarf Galaxy	0.1	10^{-4} – 10^5	Yes	W23
MHD_10_HR	AREPO	Dwarf Galaxy	0.01	10^{-5} – 10^8	Yes	New simulation
MHD_SAT_HR	AREPO	Dwarf Galaxy	0.01	10^{-5} – 10^8	Yes	New simulation
MHD_10_LR	AREPO	Dwarf Galaxy	0.1	10^{-4} – 10^4	Yes	W23
MW_RAM_1	RAMSES	Milky Way-like Galaxy	9.15	10^{-4} – 10^3	Yes	Robinson & Wadsley (2023)
MW_RAM_2	RAMSES	Milky Way-like Galaxy	9.15	10^{-4} – 10^3	Yes	Robinson & Wadsley (2023)
MWR_R1	RAMSES	MW-like Galaxy Zoom-in	0.286	10^{-4} – 10^6	Yes	Zhao et al. (2024)
MWR_R2	RAMSES	MW-like Galaxy Zoom-in	0.286	10^{-4} – 10^6	Yes	Zhao et al. (2024)

Table 2. Simulations used. In the grid codes the maximum resolution is the size of the smallest grid cell in the dense gas. For the AREPO simulations, due to the adaptive nature of the mesh, we report the cell radius at which sink particles are formed. The cell masses in the AREPO simulations are 500 M_\odot for model MHD_10_LR, 50 M_\odot for the other models from W23, and 1 M_\odot in the new high resolution models.

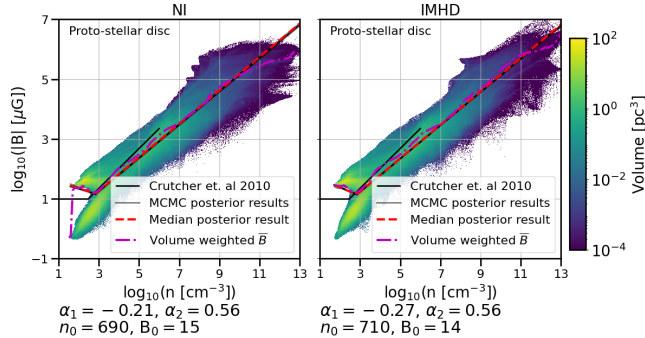


Figure 4. Core collapse to disc simulations: the volume-weighted absolute magnetic field $|\mathbf{B}|$ and number density n distribution from (left) the non-ideal and (right) the ideal MHD simulation of Lebreuilly et al. (2021). The red dashed line is the relation computed using the median parameter values inferred from the five random sample sets. The grey lines show the best-fitting relations from the five independent random samples from the data set, each consisting of 100,000 points as described in the text. These show little scatter and lie underneath the red line. The black line represents the C10 relation. The purple dashed dotted line shows the volume-weighted average B-field strength binned by density. We can see that the relation inferred from our Bayesian analysis is similar to the volume-weighted mean B-field curve, and they are both close to $\alpha_2 \simeq 0.56$. We note the values for each parameter under the related plot.

taken from the SILCC simulations of Girichidis et al. (2018) with the FLASH AMR code are shown in Figure 5. We show simulations B3 and B6, run with initial seed fields of $3 \mu\text{G}$ and $6 \mu\text{G}$, respectively. Both simulations have a base spatial resolution of 4 pc, going down to 1 pc in the densest gas, and have been run for 60 Myr.

Comparing the two simulations, we find that $n_0 < 0.5 \text{ cm}^{-3}$ and that they have a diffuse gas exponent of $\alpha_1 = 0.57$ – 0.67 . In the dense gas the exponent is reduced;

$\alpha_2 = 0.20$ in B3 and $\alpha_2 = 0.15$ in B6, in contrast to the C10 relationship.

The results shown in Figure 6 are taken from Colman et al. (2022) and Brucy et al. (2023). They used the AMR code RAMSES to compute MHD simulations in a $(1 \text{ kpc})^3$ domain. The two simulations shown include one with a uniform cell resolution of 4 pc and another with an AMR grid ranging from 4 pc in the low-density gas to 0.12 pc in the high-density. The lower and uniform resolution simulation KPC_LOW was run for 58 Myr while the AMR simulation KPC_HIGH was run for an additional 30 Myr at uniform resolution before being allowed to refine to higher resolution and run for an additional 20 Myr. The initial magnetic field in both simulations was set to $7 \mu\text{G}$.

The exponents in both the diffuse and dense gas of KPC_LOW are small, $\alpha_1 = 0.13$ and $\alpha_2 = 0.36$. In KPC_HIGH the diffuse gas exponent is larger, $\alpha_1 = 0.23$, whilst the dense gas exponent is rather lower, $\alpha_2 = 0.13$. The break occurs between $n_0 \sim 1 \text{ cm}^{-3}$ and $n_0 \sim 21 \text{ cm}^{-3}$, one to two orders of magnitude below the break expected from C10.

Figure 7 shows results from the PENCIL simulations of Gent et al. (2024) taken at various times to see the effects of the SSD and the large-scale dynamo (LSD), both of which are described in the review by Korpi-Lagg et al. (2024). These simulations include SN feedback, heating and cooling, and, in the case of the LSD simulation, vertical stratification and galactic shear. The SSD simulation has a resolution of 1 pc, while the LSD simulation has a resolution of 4 pc. We plot the B – n relationship at three times for the SSD simulation: just as the field begins to grow at 35 Myr; when the SSD begins to saturate at 98 Myr; and after the SSD has fully saturated, but before the LSD has had time to grow. We plot the LSD simulation at 3500 Myr, when the LSD is approaching saturation.

Over time, starting in the diffuse medium, a positive α_1 begins to appear. By 98 Myr (SSD_98) $\alpha_1 \sim 0.67$ with α_2

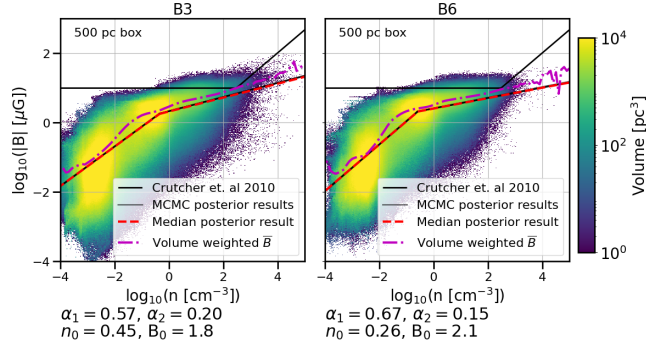


Figure 5. Stratified (0.5 kpc)³ cube simulations without shear from [Girichidis et al. \(2018\)](#) with initial field strength of (left) 3 μG and (right) 6 μG . The same notation is used as in Figure 4. All of the data in these simulations lie below the Crutcher relationship with a low power-law exponent in the denser gas, a transition at $n \sim 0.3 \text{ cm}^{-3}$, and a larger power-law exponent at low densities.

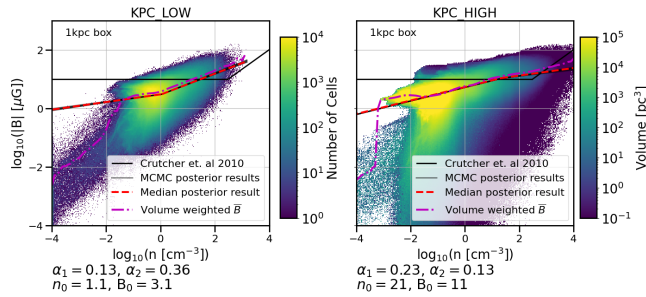


Figure 6. Stratified (1 kpc)³ cube simulations without shear. The same notation is used as in Figure 4. (Left) the uniform 4 pc resolution simulation of [Brucy et al. \(2023\)](#); (right) the AMR simulation with highest resolution of 0.12 pc of [Colman et al. \(2022\)](#). These simulations do not agree well with the C10 relationship, with only the lower resolution simulation having a larger exponent in the denser gas. There is more scatter in the results in the diffuse gas. The high-resolution simulation appears to have almost a single slope.

still slightly negative, likely a result of the initial conditions. At ~ 700 Myr (SSD_700) α_1 remains the same, ~ 0.69 , and the break density remains similar as well at $n_0 \sim 0.019 \text{ cm}^{-3}$. The LSD saturates and we see in LSD_3500 $\alpha_1 = 0.78$ and $\alpha_2 = 0.012$, with a break at a slightly higher density of $n_0 \sim 0.16 \text{ cm}^{-3}$. The value of B_0 has increased by a factor of ~ 40 , to the value of 10 μG seen in C10.

4.3 Isolated galactic simulations

4.3.1 Dwarf galaxies

Figure 8 shows data from the MHD_10 and MHD_SAT low-metallicity dwarf galaxy simulations of [W23](#), which used AREPO. MHD_10 starts with an initially weak poloidal magnetic seed field of $10^{-6} \mu\text{G}$, while MHD_SAT has an initial poloidal field of $10^{-2} \mu\text{G}$. Both simulations include self-gravity. The data are taken from the 1 Gyr snapshots.

The plots in Figure 9 show data from new, high-resolution simulations that use the MHD_10 and MHD_SAT 1 Gyr data from [W23](#) as initial conditions. We describe the new simulations in detail in Appendix B.

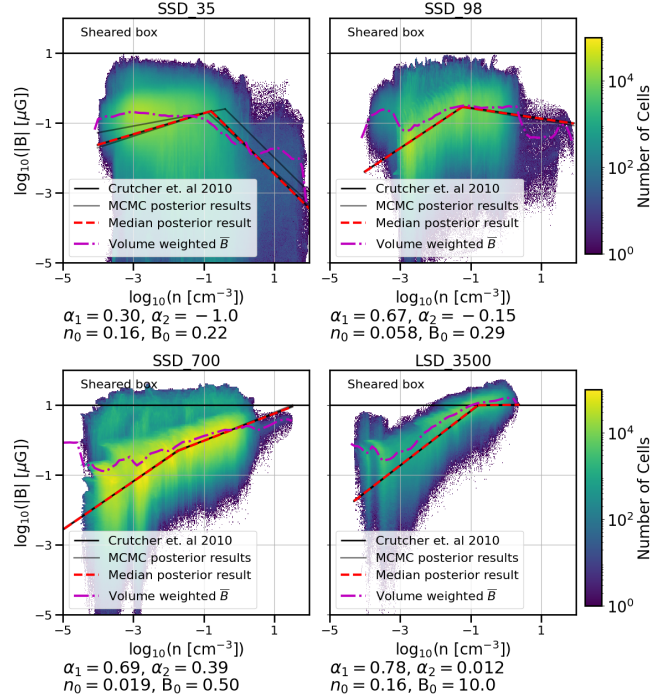


Figure 7. The volume-weighted absolute magnetic field $|\mathbf{B}|$ and number density n distribution of PENCIL simulations of galactic dynamos. We use the notation introduced in Figure 4. We show three plots where the SSD is dominant at different times from [Gent et al. \(2024\)](#), and one where the LSD has become dominant. We see the effects of the growth of the SSD on the gas from its early kinematic stage at 35 Myr to when it is fully saturated at 700 Myr. We can see at 35 Myr has a decreasing field strength in dense gas. After 98 Myr we see a rise in the exponent of the slope in the denser gas to near $|\mathbf{B}| = n^0$ and in the diffuse gas it becomes larger. After 700 Myr when the SSD and field have had time to grow and reach saturation, we see a rise in the dense gas exponent to $\alpha_2 \sim 0.39$ whilst the diffuse region remains the same. The break occurs in this simulation towards the denser gas near where there are less cells. After 3500 Myr, the LSD is dominant and we see in this case a power law of $\alpha_1 \sim 0.78$, with a turn over and flattening in the most dense gas.

MHD_10 has both exponents nearly equal, $\alpha_1 = 0.49$ and $\alpha_2 = 0.44$ with the break density occurring at $n_0 \sim 360 \text{ cm}^{-3}$. The higher initial field model MHD_SAT has lower diffuse and dense gas exponents $\alpha_1 \sim 0.33$ and $\alpha_2 \sim 0.39$.

The higher resolution dwarf galaxy model MHD_10_HR shows similar exponents to MHD_10, $\alpha_1 = 0.47$ and $\alpha_2 = 0.49$ but with the break density occurring at much higher values; $n_0 \sim 700 \text{ cm}^{-3}$. Comparison of MHD_SAT_HR to MHD_SAT shows that the higher resolution simulation has a smaller exponent in the diffuse gas $\alpha_1 \sim 0.28$, but a higher exponent in the dense gas $\alpha_2 \sim 0.54$.

4.3.2 Milky Way-type galaxies

Figure 10 presents the results for a Milky Way-like galactic MHD simulation from [Robinson & Wadsley \(2023\)](#) using RAMSES. The data is taken after 600 Myr and has a resolution on an AMR grid ranging from 36.6 pc to 9.15 pc in the densest gas. The initial magnetic field was toroidal and set at

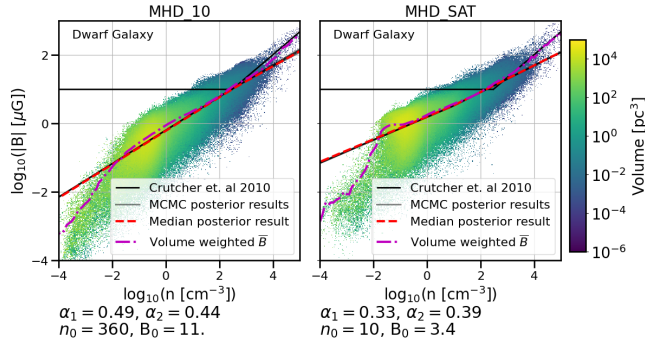


Figure 8. The volume-weighted absolute magnetic field $|\mathbf{B}|$ and number density n distribution for dwarf galaxy simulations (left) MHD_10 and (right) MHD_SAT taken from W23. The same notation is used as Figure 4. Simulation MHD_10 shows an almost uniform power-law with $\alpha_1 \sim 0.49$ and a break at the expected $n_0 \sim 360 \text{ cm}^{-3}$, whereas MHD_SAT has lower exponents in both the diffuse and dense gas with the break occurring at much higher density

either $1 \mu\text{G}$ or $0.1 \mu\text{G}$ at a number density of $n = 0.25 \text{ cm}^{-3}$. The initial power-law index of the field-density relationship was set to $\alpha = 2/3$ across the whole density range and includes self-gravity. These simulations evolve the galaxy from this initial state over a period of 250–300 Myr, by which time the disk has settled into a steady state with a star formation rate of a few solar masses per year, as observed. The field saturates to $10\text{--}20 \mu\text{G}$ by the end of the simulation.

The exponents in both simulations have lower than expected values for n_0 : 22 and 0.40 cm^{-3} respectively compared to the original Crutcher result. Both have large values for the exponent in the diffuse gas; MW_RAM_1 has $\alpha_1 \sim 0.56$ and MW_RAM_2, has $\alpha_1 \sim 0.72$. The dense gas exponent for MW_RAM_1 is $\alpha_2 \sim 0.14$ and for MW_RAM_2 is $\alpha_2 \sim 0.46$. The low value in MW_RAM_1 arises from the high density at which the break occurs and follows the volume-weighted field strength as expected.

Figure 11 shows two 3 kpc zoom-in regions of multi-scale galactic MHD simulations, using RAMSES and including SN feedback (Zhao et al. 2024). These have grid resolution of 0.286 pc with a mass refinement of 93 M_\odot and are zoom-in boxes in a Milky Way-like simulation whose setup is similar to Robinson & Wadsley (2023), including galactic shear and self-gravity. The simulations employ delayed cooling that allows superbubbles to expand for 5 Myr before being affected by cooling. The zooms focus on two different 3 kpc regions within the galaxy: the *active* region is dominated by intersecting SN-blown bubbles at a time of 283 Myr (MWR_R2) while the *quiet* region (MWR_R1) is less affected by bubbles and follows a portion of a spiral arm at 337 Myr. The dense gas is resolved to $n = 10^6 \text{ cm}^{-3}$.

The exponents vary between the two different simulation regimes. For the dense gas exponents, MWR_R1 has $\alpha_2 \sim 0.52$ while MWR_R2 has $\alpha_2 \sim 0.44$. The latter, more turbulent region, has a slightly lower value. For the diffuse gas exponent, on the other hand, there is the opposite trend: MWR_R1 has $\alpha_1 \sim 0.59$, while MWR_R2 shows $\alpha_1 \sim 0.61$.

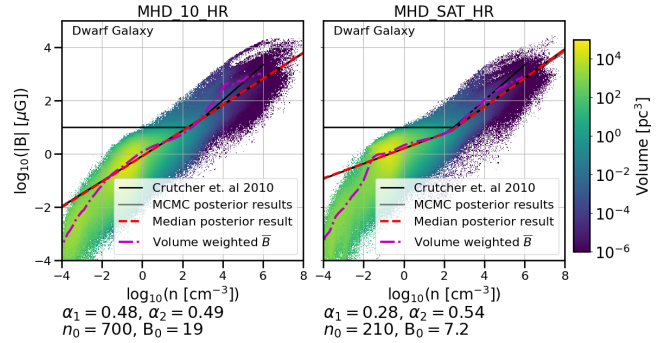


Figure 9. The volume-weighted absolute magnetic field $|\mathbf{B}|$ and number density n distribution for the new high-resolution MHD dwarf galaxy simulations (left) MHD_10_HR and (right) MHD_SAT_HR. The same notation is used as Figure 4. MHD_10_HR again shows an almost uniform power-law exponent with $\alpha \sim 0.48$ with the break at $n_0 \sim 700 \text{ cm}^{-3}$. MHD_SAT_HR shows a break at $n_0 \sim 210 \text{ cm}^{-3}$ with a small exponent in the diffuse gas, and an exponent of $\alpha_2 \sim 0.54$ in the dense gas.

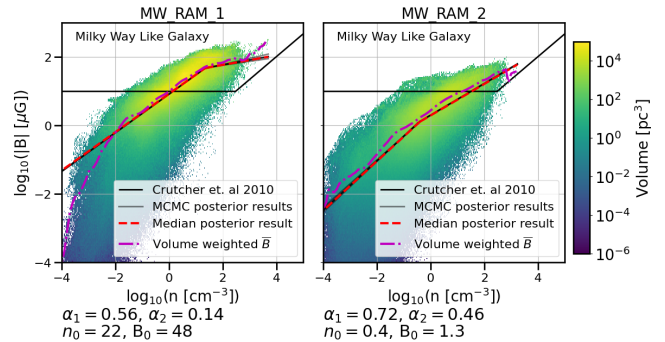


Figure 10. The volume-weighted absolute magnetic field $|\mathbf{B}|$ and number density n distribution taken from a Milky Way simulation using RAMSES from Robinson & Wadsley (2023). The same notation is used as Figure 4. (Left) a simulation with a higher initial field strength of $1 \mu\text{G}$. (Right) a simulation with a lower initial field strength of $0.1 \mu\text{G}$. Both simulations show a higher value of α_1 than α_2 , with MW_RAM_2 being the larger. MW_RAM_1 shows a large decrease in α_2 , but with a higher break density and field strength.

5 DISCUSSION

5.1 The B - n relation from observations

The original B - n relation has been a useful tool in furthering our understanding of the physics of magnetic fields in the ISM, with its implications for star formation and other processes. However, since it was developed by C10, there has been little development of the approach beyond the use of Zeeman measurements (see Tritsits et al. 2015; Jiang et al. 2020). To date, no other studies have included DCF estimates.

With our extended analysis of not only the Zeeman data, but also of 24 years of starlight and dust polarized emission observations and DCF calculations, we have found that a new form for the relation emerges, which has important consequences. We begin our discussion by considering our treatment of the original Zeeman data and how it differs from the earlier work.

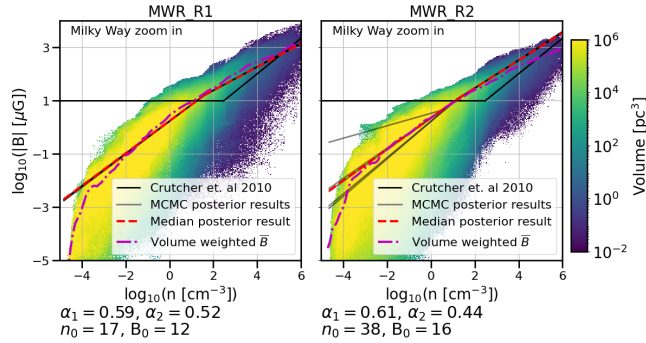


Figure 11. The volume-weighted absolute magnetic field $|B|$ and number density n distribution taken from two, 3 kpc zoom-in regions of Milky Way simulations from Zhao et al. (2024) using RAMSES: (Left) an active region dominated by superbubbles, (Right) a more quiescent region dominated by a spiral arm segment. The same notation is used as Figure 4. We see that the maximum a posteriori relation has a larger α_1 for both regions (~ 0.59 and 0.61 respectively) than α_2

Beginning with the Zeeman data set, the power-law exponents α_1 and α_2 are inconsistent with the values proposed in C10, the high-density exponent, $\alpha_2 = 0.53$ is below the original 0.66, and lies just outside the 68% credible interval. The low-density exponent α_1 appears to be well constrained with the 68% interval being relatively small. We also find that our median value for $n_0 \sim 4000 \text{ cm}^{-3}$ is much higher and not within the 68% interval of the original result.

The interpretation of a slope change at the density $n_0 \sim 300 \text{ cm}^{-3}$ given by C10 is that it is the average density at which parsec-scale clouds become self-gravitating. However, this is not a strict threshold, and the break can occur across a range of values, as our results show. The break in the B - n relation depends on a number of specific physical conditions, such as the convergence of flows, SN-driven shock fronts, and other forms of turbulence. We discuss the break in detail in Section 5.2.

The DCF data set has a two-part power law of a form similar to the Zeeman data, with a lower value of the diffuse gas exponent $\alpha_1 \sim 0.26 < \alpha_2$. Neither of these results match the $\alpha \sim 0.4$ found in Liu et al. (2022b), though they only consider a single power-law using a least-squares fit model. And much like the Zeeman data, the break occurs at a higher density and field strength, both with significant uncertainties.

What determines the exponents? Sur et al. (2012) argue that different turbulent driving processes can affect the exponent in the dense gas. For example SNe, shear, or gravitational collapse could all affect the exponents. Another possibility is the Alfvénic Mach number and whether the gas is magnetically super-critical or not (Li et al. 2013; Mocz et al. 2017; Myers & Basu 2021; Auddy et al. 2022). The higher the magnetic field, the less super-critical the gas, the lower the diffuse gas exponent and the sharper the difference between the two exponents becomes (Mocz et al. 2017).

Our most interesting finding is the similarity of both exponents in the two data sets, with both exponents derived from the Zeeman measurements being close to the DCF results, showing that the DCF data can be used to approximate a relationship despite its issues. A more detailed study of the diffuse exponent, including detailed error treatment, would

provide valuable insights. Its value likely probes the dynamical nature of magnetic field generation in diffuse gas. We shall discuss this in more detail in the context of numerical simulations in Section 5.3.

5.2 The observational break density

One of the most notable differences between our work and previous studies is the inference of a new free parameter α_1 for the power-law of the relationship in diffuse gas. Adding α_1 changes key aspects of the original relationship, most importantly, the value of the break density n_0 .

Figure 12 shows the marginal distributions for n_0 from our hierarchical Bayesian analyses for the Zeeman and DCF data set. The estimated n_0 for both is significantly different from that predicted by C10. The Zeeman data implies $n_0 \sim 4000 \text{ cm}^{-3}$, a full decade higher than the C10 result. One reason for this could be the way the Zeeman data are distributed. Recall that the Zeeman data are derived using the line emission from three distinct species that sample different density ranges. One problem that arises from this is that there are two distinct gaps in the data, one around $n = 10^3 \text{ cm}^{-3}$ and one at $n \sim 5 \times 10^4 \text{ cm}^{-3}$ that separate the three surveys. A result of this is that 100 of the 137 observations lie below $n = 4000 \text{ cm}^{-3}$. This skew to lower densities could bias the fit due to clumpy, non-randomly sampled distribution of density measurements. These variations in the distribution of the Zeeman data over n could then contribute to the uncertainty in the break density. To better constrain the break in the Zeeman data we need better sampling of the density range.

The DCF data implies $n_0 \sim 1.4 \times 10^5 \text{ cm}^{-3}$, a break density much higher than that inferred from the Zeeman value. The DCF data also have a much higher value of n_0 than the original Zeeman results reported in C10, which does not fall within our 68% credible interval. The distribution of the DCF data is quite even across decades of n and therefore the inferred break density from the DCF data is likely more trustworthy. What could be driving this high n_0 value?

The ISM is a multiphase environment impacted by many different physical processes. Interestingly, densities of $n_0 \sim 10^5$ are the point at which dense star-forming cores begin to form. So the gas here is likely to be beginning to undergo rapid collapse to form protostars. Many observations of DCF at this density and higher are in dense cores. It has been shown recently (Ibáñez-Mejía et al. 2022; McGuiness et al. 2025), that at high densities magnetic energy becomes less dominant and the kinetic energy becomes more important. This reduction in the relative importance of the field in supporting gas against collapse could be a reason for the break to occur at higher densities.

There are observational examples of regions where stellar feedback produces a B - n scaling that is above the reported trends. Troland et al. (2016) report field strengths three to five times above the mean at comparable densities toward the atomic photon-dominated region that lies just in front of the Trapezium stars of Orion. Joubaud, T. et al. (2019) estimate enhanced B -field strengths using DCF toward the lower rim of the Orion-Eridanus superbubble. Due to the scarcity of observational data, these particular local conditions cannot be easily marginalized to identify a single physical cause or a value for the break density. Soler & Hennebelle (2017) show that a negative velocity divergence can cause a change in

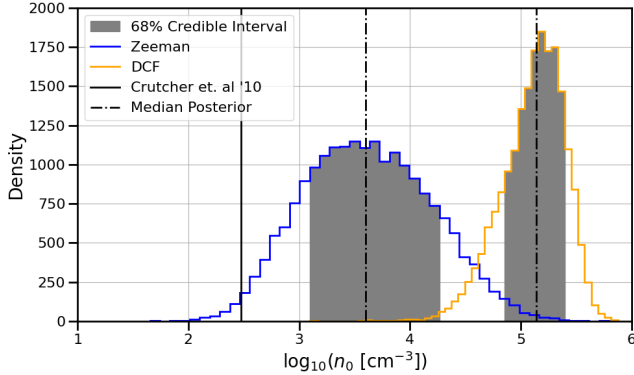


Figure 12. Marginal posterior distributions for n_0 for the Zeeman (blue) and DCF (orange) data sets. The shaded regions show the 68% credible intervals, the dashed-dotted lines show the posterior medians, and the solid black line shows the prediction from C10. Neither distribution favours the latter result.

field orientation in observations at around the original break density and conclude that this could arise for multiple reasons, i.e. gravitational collapse, external pressure from the warm medium, or colliding flows. These degeneracies could also lead to changes in the break density.

Our results suggest that the B - n scaling is strongly tied to the specific environment, and if so, more extended surveys of field strengths are needed to further conclude on generality of a critical density.

5.3 The B - n relation from numerical simulations

In this subsection, we discuss the B - n relations drawn from our various simulations and reasons for the deviations seen in each case.

5.3.1 Core collapse simulations

These simulations are of sufficiently high resolution to capture the formation of protostellar discs, which are much denser than typical regions in molecular clouds, as we see in Figure 4, where $n = 10^{13} \text{ cm}^{-3}$ is reached. The negative α_1 is due to numerical scatter in the most diffuse gas. These simulations do not trace gas below $\sim 500 \text{ cm}^{-3}$. This would technically prevent us from drawing conclusions on the diffuse gas exponent and break density suggested by C10. However, comparing with our new observational results we do not find a break at the higher densities. This could be due to the result of focusing on the discs in the model.

Protostellar discs are born in an environment undergoing compression through gravitational collapse. This leads to the field dynamically constraining the collapse along field lines, which gives rise to $\alpha_2 \sim 0.56$. We see no difference in the value between simulations with and without ambipolar diffusion, although we note the presence of a plateau at high density (in a negligible fraction of the volume) for the case with ambipolar diffusion.

5.3.2 Stratified Box simulations

The two $(0.5 \text{ kpc})^3$ stratified box simulations of Girichidis et al. (2018) shown in Figure 5 only differ in initial seed field strength. They reach high enough densities that a break at $n_0 = 300 \text{ cm}^{-3}$ could appear, but it actually appears at lower values of, $n_0 \sim 0.45 \text{ cm}^{-3}$ and $n_0 \sim 0.26 \text{ cm}^{-3}$. The diffuse exponent is high whilst the dense exponent is much lower than expected.

There are two possible reasons for this result. The first is that the diffuse gas is more turbulent than the dense gas as the simulation is being driven by strong supernova (SN) feedback. Gent et al. (2021) report that the SSD grows rapidly in hot, diffuse gas, so the high sound speeds provided by SN shock heating accelerate field growth. This suggests that not enough SN heating has occurred to allow for the growth of the SSD. The second explanation is that these simulations have run for only 60 Myr, meaning the dynamo has likely not reached saturation and the field is likely still growing. The SSD can take a few tens to hundreds of megayears to saturate depending on numerical resolution (Gent et al. 2021; Whitworth et al. 2023; Gent et al. 2024).

Unsaturated fields in these simulations have important effects. With values significantly below saturation, the magnetic pressure support is reduced, allowing the gas to collapse faster. Starting with a higher field (see simulation B6, Fig. 5) does not seem to counteract this. As the gas is not hot or turbulent in the initial conditions, the field does not dynamically support the gas. Figure 3 of Robinson & Wadsley (2023) shows their high initial field strength simulation decreasing in field strength over time meaning an artificially high field may not be able to counteract this effect and that allowing a field to evolve naturally, or begin near saturation is a better solution.

The simulations in Figure 6 have been run for a longer time than those in Figure 5. Both show small exponents in both the diffuse and dense gas, which means that evolutionary time could have an effect. The gas is hot and turbulent enough for the SSD to grow. However, when the resolution is increased in KPC_HIGH and the simulation is run longer, we see a smaller exponent in the diffuse gas.

Again, there are a few reasons why this could be happening. One is the change in resolution, as discussed in Section 5.3.4. Since the saturation time for the SSD depends sensitively on numerical resolution down to sub-parsec scales (Gent et al. 2021), a sudden change in resolution will lead to a change in the rate of field amplification. As KPC_HIGH was only run for an additional ~ 20 Myr at higher resolution, this may not be long enough for the B field to saturate at the new resolution, leaving the field strength low at high densities.

Another key factor in determining the exponents are the initial conditions. Sur et al. (2012) showed that varying the turbulent driving can lead to a departure from the dense gas exponent $\alpha_2 = 2/3$. It becomes smaller as the SSD saturates first on small scales, and later at larger scales. Gent et al. (2021) shows that the SSD grows rapidly in a hot turbulent medium. Most simulations start with the gas uniform in temperature and density. Therefore, if simulations are initiated with specific seed field configurations, then the magnetic field in the diffuse medium will likely drop due to a lack of a hot, turbulent phase.

Another possible cause for the slopes to arise in the SSD

and LSD models that specifically lack self-gravity could be due to equipartition between the magnetic and kinetic energies. This would introduce an additional variable into relationship, the dependence on gas velocity changing it from $B \propto n^\alpha$ to $B \propto n^\alpha \times v$. However to fully test this new form is beyond the scope of this work.

Important processes are missing from these simulations. In particular, galactic rotation and shear are key in the growth of the LSD in galaxies, which offers large-scale support to the field over much longer time-scales. On shorter time scales shear may affect the gas distribution through large-scale rotational effects. We consider these processes in the next subsection.

5.3.3 Galactic rotation

The dwarf galaxy simulations of W23, shown in Figure 8, have a range in density of $n = 10^{-4}$ – 10^5 cm $^{-3}$, comparable to that covered by the Zeeman observations. We see that MHD_SAT has smaller exponents in both diffuse and dense gas than MHD_10, though in both cases the diffuse and dense exponents are similar. This suggests that the relationship is connected to the initial conditions. We confirm this by noting that MHD_SAT has a larger initial seed field, 10^{-2} μ G, which, as seen in Figure 5 of W23, results in a field with large-scale order and higher strength in the diffuse regions.

If a simulation is initiated with a stronger field then the gas is dynamically supported for longer. This leads to the diffuse gas starting with a higher field, giving rise to a lower value for α_1 . This is in contrast to the stratified box simulations and is likely an effect of numerical resolution, with the stratified box simulations having rather higher resolution, allowing them to model faster growth of fields from small scales to saturation at large scales.

Figure 10 shows the results from a Milky Way-scale simulation. As in the case of the dwarf galaxy simulations, the diffuse gas field strength has dropped below the initial field strength. This suggests the SSD is not active enough to amplify the field here. This may be a resolution problem, as the diffuse gas is under-resolved, meaning the SSD cannot be accurately modelled (see Martin-Alvarez et al. 2022, for discussion of this issue). We discuss this in Section 5.3.4 below.

Figure 2 in Robinson & Wadsley (2023) compares the time evolution of the B - n relationship for different initial field strengths. In the case of a weak or medium initial seed field, α_2 tends to 0.5. In the strong field case, MW_RAM_1, the diffuse gas exponent rises to $\alpha_1 = 0.56$ but α_2 drops significantly to 0.14. However, in the weak field case both α_1 and α_2 grow from the initial conditions. The important point here is that simulations with weak initial fields grow naturally by dynamo action resulting in the best fits to the observations. Imposing artificially strong initial fields has adverse effects on star formation and the final saturated state of the field.

Large-scale dynamo action in Milky Way-scale galaxies depends on rotational time scales, which are much longer than the eddy time on which the SSD grows. It is expected to take of the order of 5–10 rotations (Pfrommer et al. 2022; Gent et al. 2024) for the LSD to become the dominant source of magnetic field support. The rotational period of the dwarf galaxies is on the order of 400 Myr (W23), with a similar dynamical time in the simulations of Robinson & Wadsley

(2023). As these simulations only run for 1 Gyr, this likely means that LSD effects are not yet dominant.

The simulations in Figure 7 by Gent et al. (2021) and Gent et al. (2024) track the effects of dynamo evolution over 3.5 Gyr. We see that as the dynamo evolves from the SSD in the early stages (~ 35 Myr) to the LSD at late times (~ 3500 Myr), the diffuse exponent characterizing the bulk of the gas tends to high values, $\alpha_1 \sim 0.78$. This could point to the denser and more turbulent gas in these models amplifying the field quicker. Although we cannot say much about the dense gas exponent from these simulations, as they do not trace a density range high enough, we can be confident in saying that the diffuse gas has a non-zero exponent and that this arises purely from dynamo activity; these simulations do not include self-gravity, implying that their B - n relation is purely driven by dynamo activity driven, feedback and shear.

In summary, we have shown that all simulations that include large scale galactic rotation tend towards an exponent of ≥ 0.5 . This can appear in either the diffuse gas exponent α_1 or the dense gas exponent α_2 in the results depending on the set up of the simulation and density range captured. We also see that the dwarf galaxy simulations and the Milky Way-like simulations are most similar to the observational results. This is one of our most important results. It suggests that shear and dynamo processes on galactic scales, rather than gravitational collapse, can shape the multi-scale B - n relation.

5.3.4 Resolution effects on the dynamo

Using high resolution zoom-in MHD simulations of clouds embedded in a stratified box with SN driving, Ibáñez-Mejía et al. (2022) showed that molecular clouds have magnetically supported envelopes with a field perpendicular to the density gradient. In all three clouds they simulate, each has an exponent of less than $\alpha = 0.5$ with no break in the B - n relationship. However, the diffuse gas is poorly resolved in these AMR simulations.

Indeed, most numerical simulations of the ISM on large scales lack resolution in diffuse gas. Of the simulations presented here, two resolve the diffuse gas to scales where the SSD should be captured: the dynamo simulation of Gent et al. (2024), SSD_35, SS_98, and SSD_700, with a uniform 1 pc resolution, and the Milky Way-like zoom-in simulation of Zhao et al. (2024), with a uniform 0.29 pc resolution. This is important as the SSD must be resolved down to 1 pc or better scales to accurately capture its growth rate (Korpi-Lagg et al. 2024). Resolving the SSD is important in order to track the rapid amplification intrinsic to turbulent dynamo theories. This could lead to a stronger field in the diffuse gas adding support and slowing its transport to denser regions.

In the time-evolving SSD PENCIL simulation (Fig. 7), α_1 tends towards a larger than expected value of 0.78. This is a stratified box simulation with shear, not a full galactic disc, but it does have a dense mid-plane with diffuse gas bubbles (see Figures 1, 3 and 13 in Gent et al. 2024). This shows that given enough time, on the order of a few hundred megayears, in a simulation with a rotation rate twice that of the Milky Way (so around 5 rotation periods), along with shear, an exponent exceeding 0.5 in the diffuse gas can arise.

The high resolution dwarf galaxy simulations MHD_10_HR and MHD_SAT_HR (Fig. 9) have lit-

tle difference in the low density exponents compared to the original simulations of W23 (Fig. 8). This is due to the diffuse gas still not being well resolved, only reaching parsec scale resolution at $n > 10 \text{ cm}^{-3}$. However, in the dense gas for MHD_SAT_HR we find the exponent has increased, matching the observed Zeeman result. This model includes photoionisation feedback and high resolution at the highest densities and has had an ordered LSD for longer than other models. This shows that the more complete the model, the more likely we are to approach the observed results. When we look at the lowest resolution dwarf galaxy simulation, MHD_10_LR, we see a large departure from the results in the more resolved simulations. Appendix C focuses on the resolved diffuse gas in the dwarf galaxy simulations.

The zoom in regions of Zhao et al. (2024) shown in Figure 11 have a similar exponent in both the dense and diffuse gas. However, the turbulent region, MWR_R2, has a larger exponent in the diffuse gas, which supports the idea that turbulence is driving the relationship.

Thus, we have found that the simulations that match our observational results the closest are, primarily the high-resolution dwarf galaxy simulation MHD_SAT_HR, followed by MHD_10_HR and MWR_R1. These are all high resolution simulations best able to trace both diffuse and dense gas meaning they are more able to accurately model both the small and large scale dynamos.

In summary, by considering the ensemble of simulations presented here, a major finding is that the more physically complete a simulation is, the more closely the exponents in the relationship match the observed exponents. In addition, this match is better when simulations are allowed to evolve for a sufficiently long time, when they spatially resolve both the diffuse and dense phases, and when they include galactic rotation or shear as well as stellar feedback mechanisms.

5.4 The numerical break density

Only a few of the simulations presented here allow us to confidently draw any conclusions about the break density n_0 , due to the density ranges they cover. Simulations that do not span a density range above or below $n \simeq 100 \text{ cm}^{-3}$ (where gas becomes dense) by a few orders of magnitude will likely give misleading results. For example, in the protoplanetary disc population simulations NI and IMHD, we find $n_0 \sim 700 \text{ cm}^{-3}$ which is close to the lowest density. Conversely, the PENCIL simulations don't achieve densities of $n_0 \sim 300 \text{ cm}^{-3}$ meaning no break is likely to be found at the expected density.

Over all, we find much variability in the value of the break density for the simulations that span the density range of the observational data sets. These are the simulations KPC_HIGH, MHD_10, MHD_SAT, MHD_10_HR, MHD_SAT_HR, MWR_R1, MWR_R2, and possibly B3 and B6. The lowest n_0 found in these simulations is $n_0 \simeq 17 \text{ cm}^{-3}$ in MWR_R2, whilst the highest is $n_0 \simeq 700 \text{ cm}^{-3}$ in MHD_10_HR—a difference of an order of magnitude.

Of these simulations, only the top of the 68% credible interval of MHD_10_HR comes close to the lower end of the Zeeman 68% credible interval, whilst MHD_SAT_HR and MHD_10 are close to the C10 break density of $n_0 = 300 \text{ cm}^{-3}$. The values for B_0 are just as variable with numbers ranging from $B_0 \sim 0.094 \mu\text{G}$ in MHD_10_LR to $B_0 \sim 48 \mu\text{G}$ in MW_RAM_1.

The numerical break density appears to depend on several key factors, including numerical resolution, initial seed field strength, and the runtime of the simulation. To better constrain the break point in numerical simulations we need better estimates on the errors. We may also need to resolve the dense gas phase even more carefully. If, for example, the reason for the break in the DCF data is due to dense core formation, then this would need to be fully resolved with accurate feedback models that include winds and jets generated by the protostellar objects. We leave this for future studies.

5.5 Numerical caveats

A consideration for any numerical simulation is the effect of numerical diffusion as a result of finite resolution. In magnetic field studies this is particularly important because of the effects at small scales where resistivity becomes important. None of the simulations presented here are resolved well enough to completely overcome this. We can, however, consider what happens when resolution is improved (Fig. 13). MHD_10_LR is taken from the Appendix of W23 and has a much lower resolution than MHD_10 with a Jeans refinement of 4 cells instead of 8, a cell mass of 500 M_\odot , and a sink creation density threshold of 10^2 cm^{-3} . Whilst the dense gas exponent is $\alpha_2 \sim 0.52$, the diffuse exponent becomes much larger, $\alpha_1 \sim 0.84$. As we increase the resolution up to the high resolution simulation MHD_10_HR, α_1 tends to ~ 0.49 .

Another caveat is that the simulation results do not typically have errors. We have attempted to rectify this by implementing errors based on the KDE method as described in Appendix A4. Comparing the results of from Bayesian inference to the volume weighted average magnetic field binned via density in each numerical simulation in Figures 4, 5, 6, 7, 8, 9, 10 and 11, we see that they match quite closely. By including the nuisance factor $\ln V$ in the model we mitigate some of the issues that arise due to poor error treatment.

6 SUMMARY AND CONCLUSIONS

By analysing two observational data sets—the original Zeeman data of C10 and a large sample of DCF measurements—within a hierarchical Bayesian framework that allows both exponents in the power-law relation to vary freely, we have comprehensively treated the B - n relation.

Our results differ from those found by C10. This is most clearly seen in the non-zero power-law exponent for the diffuse gas as well as in the values of the break density n_0 and magnetic field B_0 . The break density n_0 in the DCF results is roughly comparable to that of dense star forming cores, $\simeq 10^5 \text{ cm}^{-3}$. However, the ISM is highly anisotropic and without further more detailed study the exact reason for the break here is difficult to determine.

We performed a similar analysis on nineteen numerical simulations that result in a wide range of parameters for the B - n relation. The results are highly dependent on the system being studied. For simulations to reproduce the observed results, a turbulent galactic dynamo must resolve both the diffuse and dense gas (requiring a spatial resolution below 1–2 pc) and be run over sufficiently long time scales (a few hundred megayears) to bring an initially weak magnetic field

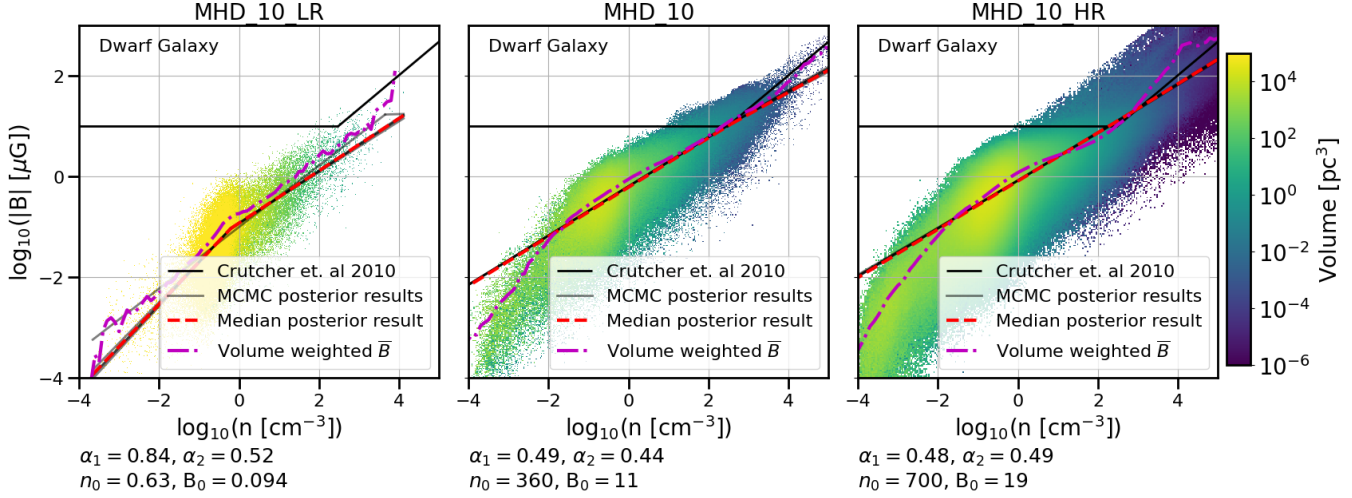


Figure 13. The $|\mathbf{B}| - n$ distribution for three dwarf galaxy simulations with varying numerical resolution: the low resolution dwarf galaxy simulation from the Appendix of W23, MHD_LR, MHD_10, and the new high-resolution MHD_10_HR. The same notation is used as Figure 4. This comparison shows the effects of numerical diffusion. As the simulation becomes more resolved, the relationship for both exponents tends to $\alpha_1 \simeq \alpha_2 \simeq 0.5$.

up to a saturated, steady-state value in the ISM. Thus, it appears that the relation is not strongly tied to the self-gravity of the system. Rather, it is driven by the dynamo, feedback, and turbulence.

We summarise our key findings:

- We find a two-part power-law relation differing from that found by C10 for the observational data:

$$|\mathbf{B}| = B_0 \begin{cases} \left(\frac{n}{n_0}\right)^{\alpha_1} & \text{if } n \leq n_0, \\ \left(\frac{n}{n_0}\right)^{\alpha_2} & \text{if } n > n_0. \end{cases} \quad (3)$$

- The parameters for the Zeeman data are $B_0 = 950_{-50}^{+610} \mu\text{G}$, $n_0 = 4.00_{-2.9}^{+12.7} \times 10^3 \text{ cm}^{-3}$, $\alpha_1 = 0.15_{-0.09}^{+0.06}$, and $\alpha_2 = 0.53_{-0.07}^{+0.09}$.
- The DCF data that has reported errors in Pattle et al. (2022) results in parameters $B_0 = 416_{-104}^{+117} \mu\text{G}$, $n_0 = 13.9_{-7.30}^{+10.1} \times 10^4 \text{ cm}^{-3}$, $\alpha_1 = 0.26_{-0.15}^{+0.15}$, and $\alpha_2 = 0.77_{-0.15}^{+0.14}$.
- The observed exponent in the diffuse gas $\alpha_1 > 0$ in all cases.
- The observed break density occurs at substantially higher densities than found by C10, although with large error bars reflecting the highly variable dynamical and anisotropic state of the ISM.
- The high resolution dwarf galaxy simulations match the observed power-law exponents most closely, while the other full galaxy simulations also give good results.
- We find clear evidence that the less approximate the simulations are the more likely they are to match the observed $B - n$ relation. Important improvements include higher spatial resolution, inclusion of shear and other dynamical processes, and long enough run times to accommodate dynamo saturation and other turbulence related effects.

To make further progress, we require more data from both observations and numerical simulations. It is exciting that Zeeman observations (Thompson et al. 2019; Hwang et al. 2024), Faraday rotation, and synchrotron polarization observations in the epoch of the Square Kilometer Array will offer new insights into the diffuse gas. The rapidly increasing dy-

namical range of galactic, multiscale MHD simulations is also promising.

ACKNOWLEDGEMENTS

We thank the members of the AREPO ISM group and ECO-GAL Large Scale Structures group for discussions and insightful comments on the coding and science goals in this paper. The anonymous referee provided a very useful report that helped us to improve the manuscript. We also thank V. Springel for access to AREPO and R. Treß for the development of the photoionization code used in this work. DJW acknowledges support from the Programa de Becas Posdoctorales of the Dirección General de Asuntos del Personal Académico of the Universidad Nacional Autónoma de México (DGAPA,UNAM,Mexico). SS acknowledges support from UNAM-PAPIIT Program IA10484. REP is supported by a Discovery Grant from NSERC, Canada. He is also grateful for support of his sabbatical leave in Heidelberg (2022/23), by the Institute for Theoretical Astrophysics of the University of Heidelberg (ITA) and the Max Planck Institute for Astronomy, where this work was started. RJS gratefully acknowledges an STFC Ernest Rutherford fellowship (grant ST/N00485X/1). M-MML acknowledges direct support from US National Science Foundation grants AST18-15461 and AST23-07950, as well as support from grant PHY23-09135 to the Kavli Institute for Theoretical Physics. LSV was supported by the Science Pathways Scholars Program of Barnard College. RP acknowledges funding support from Ontario Graduate Scholarships and the Queen Elizabeth II Graduate Scholarship in Science & Technology. AP acknowledges financial support from the grant UNAMPAPIIT IG100223, the Sistema Nacional de Investigadores of CONAHCyT, and from the CONAHCyT project number 86372 of the ‘Ciencia de Frontera 2019’ program, entitled ‘Cítlalcoatl: A multiscale study at the new frontier of the formation and early evolution of stars and planetary systems’, México.

DJW, PG, NB, UL, PH, RSK, and JDS acknowledge funding from the European Research Council via the ERC Synergy Grant “ECOGAL” (project ID 855130). RSK is grateful to the German Excellence Strategy for funding via the Heidelberg Cluster of Excellence “STRUCTURES” (EXC 2181-390900948), and to BMWK for support in project “MAINN” (funding ID 50OO2206). The team in Heidelberg acknowledges computing resources provided by *The Län* and DFG through grants INST 35/1134-1 FUGG and 35/1597-1 FUGG, data storage at SDS@hd funded through grants INST 35/1314-1 FUGG and INST 35/1503-1 FUGG, as well as computing resources provided by the Leibniz Rechenzentrum via grants pr32lo, pr73fi and GCS large-scale project 10391. RSK thanks the 2024/25 Class of Radcliffe Fellows for highly interesting and stimulating discussions.

DJW also personally thanks RP and MM for the initial discussions that lead to the paper and SS and GE for help in coding the Bayesian routine and discussions on the statistical implications and implementation.

This work used the DiRAC COSMA Durham facility managed by the Institute for Computational Cosmology on behalf of the STFC DiRAC HPC Facility (www.dirac.ac.uk). The equipment was funded by BEIS capital funding via STFC capital grants ST/P002293/1, ST/R002371/1 and ST/S002502/1, Durham University and STFC operations grant ST/R000832/1. DiRAC is part of the National e-Infrastructure. The research conducted in this paper used SciPy ([Virtanen et al. 2020](#)), NumPy ([van der Walt et al. 2011](#)), and matplotlib ([Hunter 2007](#)).

DATA AVAILABILITY

The dwarf galaxy data is available upon request to the first author. For all other data the reader will need to contact the owner of that data as listed in the appropriate reference.

REFERENCES

Angarita Y., Versteeg M. J. F., Havercorn M., Marchal A., Rodrigues C. V., Magalhães A. M., Santos-Lima R., Kawabata K. S., 2024, *AJ*, **168**, 47

Auddy S., Basu S., Kudoh T., 2022, *ApJ*, **928**, L2

Banerjee R., Vázquez-Semadeni E., Hennebelle P., Klessen R. S., 2009, *MNRAS*, **398**, 1082

Beck R., 2015, *A&ARv*, **24**, 4

Brandenburg A., Dobler W., 2002, *Computer Physics Communications*, **147**, 471

Brandenburg A., et al., 2020, *Journal of Open Source Software*, **6**, 7

Brucy N., Hennebelle P., Colman T., Iteanu S., 2023, *A&A*, **675**, A144

Cao Z., Li H.-b., 2023, *ApJ*, **946**, L46

Carilli C. L., Taylor G. B., 2002, *ARA&A*, **40**, 319

Chandrasekhar S., Fermi E., 1953, *ApJ*, **118**, 113

Chen C.-Y., Li Z.-Y., Mazzei R. R., Park J., Fissel L. M., Chen M. C. Y., Klein R. I., Li P. S., 2022, *MNRAS*, **514**, 1575

Colman T., et al., 2022, *MNRAS*, **514**, 3670

Commerçon B., González M., Mignon-Risse R., Hennebelle P., Vaytet N., 2022, *A&A*, **658**, A52

Crutcher R. M., 2004, in Uyaniker B., Reich W., Wielebinski R., eds, *The Magnetized Interstellar Medium*. pp 123–132

Crutcher R. M., 2012, *ARA&A*, **50**, 29

Crutcher R. M., Nutter D. J., Ward-Thompson D., Kirk J. M., 2004, *ApJ*, **600**, 279

Crutcher R. M., Wandelt B., Heiles C., Falgarone E., Troland T. H., 2010, *ApJ*, **725**, 466

Davis L., 1951, *Physical Review*, **81**, 890

Elia D., et al., 2017, *MNRAS*, **471**, 100

Foreman-Mackey D., Hogg D. W., Lang D., Goodman J., 2013, *PASP*, **125**, 306

Fryxell B., et al., 2000, *ApJS*, **131**, 273

Gelman A., Rubin D. B., 1992, *Statistical Science*, **7**, 457

Gent F. A., Mac Low M.-M., Käpylä M. J., Singh N. K., 2021, *ApJ*, **910**, L15

Gent F. A., Mac Low M.-M., Korpi-Lagg M. J., 2024, *ApJ*, **961**, 7

Girichidis P., Seifried D., Naab T., Peters T., Walch S., Wünsch R., Glover S. C. O., Klessen R. S., 2018, *MNRAS*, **480**, 3511

Girma E., Teyssier R., 2023, arXiv e-prints, [p. arXiv:2311.10826](https://arxiv.org/abs/2311.10826)

Heitsch F., Zweibel E. G., Mac Low M.-M., Li P., Norman M. L., 2001, *ApJ*, **561**, 800

Hennebelle P., Banerjee R., Vázquez-Semadeni E., Klessen R. S., Audit E., 2008, *A&A*, **486**, L43

Hennebelle P., Commerçon B., Lee Y.-N., Charnoz S., 2020, *A&A*, **635**, A67

Hildebrand R. H., Kirby L., Dotson J. L., Houde M., Vaillancourt J. E., 2009, *ApJ*, **696**, 567

Houde M., Vaillancourt J. E., Hildebrand R. H., Chitsazzadeh S., Kirby L., 2009, *ApJ*, **706**, 1504

Hull C. L. H., Zhang Q., 2019, *Frontiers in Astronomy and Space Sciences*, **6**, 3

Hunter J. D., 2007, *Computing in Science Engineering*, **9**, 90

Hwang J., Lee C. W., Kim J., Chung E. J., Kim K.-T., 2024, arXiv e-prints, [p. arXiv:2408.10506](https://arxiv.org/abs/2408.10506)

Ibáñez-Mejía J. C., Mac Low M.-M., Klessen R. S., 2022, *ApJ*, **925**, 196

Jiang H., Li H.-b., Fan X., 2020, *ApJ*, **890**, 153

Joubaud T., Grenier, I. A., Ballet, J., Soler, J. D. 2019, *A&A*, **631**, A52

Kirk H., Klassen M., Pudritz R., Pillsworth S., 2015, *ApJ*, **802**, 75

Konstantinou A., Ntormousi E., Tassis K., Pallottini A., 2024, arXiv e-prints, [p. arXiv:2402.10268](https://arxiv.org/abs/2402.10268)

Könyves V., et al., 2015, *A&A*, **584**, A91

Korpi-Lagg M. J., Mac Low M.-M., Gent F. A., 2024, arXiv e-prints, [p. arXiv:2401.04015](https://arxiv.org/abs/2401.04015)

Lazarian A., 2020, *ApJ*, **902**, 97

Lebreuilly U., Hennebelle P., Colman T., Commerçon B., Klessen R., Maury A., Molinari S., Testi L., 2021, *ApJ*, **917**, L10

Li H.-b., Fang M., Henning T., Kainulainen J., 2013, *MNRAS*, **436**, 3707

Li J., Jiang B., Zhao H., Chen X., Yang Y., 2024, arXiv e-prints, [p. arXiv:2402.10431](https://arxiv.org/abs/2402.10431)

Li J., et al., 2019, *ApJ*, **877**, 43

Liu J., Zhang Q., Commerçon B., Valdivia V., Maury A., Qiu K., 2021, *ApJ*, **919**, 79

Liu J., Zhang Q., Qiu K., 2022a, *Frontiers in Astronomy and Space Sciences*, **9**, 943556

Liu J., Qiu K., Zhang Q., 2022b, *ApJ*, **925**, 30

Mac Low M.-M., Klessen R. S., 2004, *Rev. Mod. Phys.*, **76**, 125

Martin-Alvarez S., Devriendt J., Slyz A., Sijacki D., Richardson M. L. A., Katz H., 2022, *MNRAS*

Masson J., Chabrier G., Hennebelle P., Vaytet N., Commerçon B., 2016, *A&A*, **587**, A32

McGuiness R., Smith R. J., Whitworth D. J., 2025, *MNRAS*

Mestel L., 1966, *MNRAS*, **133**, 265

Mocz P., Burkhardt B., Hernquist L., McKee C. F., Springel V., 2017, *ApJ*, **838**, 40

Molina F. Z., Glover S. C. O., Federrath C., Klessen R. S., 2012, *MNRAS*, **423**, 2680

Moscadelli L., Sanna A., Beuther H., Oliva A., Kuiper R., 2022, *Nature Astronomy*, **6**, 1068

Myers P. C., Basu S., 2021, *ApJ*, **917**, 35
 Ossenkopf V., Henning T., 1994, *A&A*, **291**, 943
 Ostriker E. C., Stone J. M., Gammie C. F., 2001, *ApJ*, **546**, 980
 Palau A., et al., 2021, *ApJ*, **912**, 159
 Passot T., Vázquez-Semadeni E., 2003, *A&A*, **398**, 845
 Pattle K., Fissel L., Tahani M., Liu T., Ntormousi E., 2022, *arXiv e-prints*, p. arXiv:2203.11179
 Pfrommer C., Werhahn M., Pakmor R., Girichidis P., Simpson C. M., 2022, *MNRAS*, **515**, 4229
 Pillai T., Kauffmann J., Tan J. C., Goldsmith P. F., Carey S. J., Menten K. M., 2015, *The Astrophysical Journal*, **799**, 74
 Planck Collaboration et al., 2016, *A&A*, **586**, A138
 Pudritz R. E., Klassen M., Kirk H., Seifried D., Banerjee R., 2014, in Petit P., Jardine M., Spruit H. C., eds, *Magnetic Fields throughout Stellar Evolution* Vol. 302, *Magnetic Fields throughout Stellar Evolution*. pp 10–20, doi:10.1017/S174392131400163X
 Robinson H., Wadsley J., 2023, *arXiv e-prints*, p. arXiv:2310.15244
 Seifried D., Walch S., Weis M., Reissl S., Soler J. D., Klassen R. S., Joshi P. R., 2020, *MNRAS*, **497**, 4196
 Skalidis R., Tassis K., 2021, *A&A*, **647**, A186
 Skalidis R., Sternberg J., Beattie J. R., Pavlidou V., Tassis K., 2021, *A&A*, **656**, A118
 Soler J. D., 2019, *A&A*, **629**, A96
 Soler J. D., Hennebelle P., 2017, *A&A*, **607**, A2
 Soler J. D., et al., 2016, *A&A*, **596**, A93
 Springel V., 2010, *MNRAS*, **401**, 791
 Sur S., Federrath C., Schleicher D. R. G., Banerjee R., Klassen R. S., 2012, *MNRAS*, **423**, 3148
 Teyssier R., 2002, *A&A*, **385**, 337
 Thompson K. L., Troland T. H., Heiles C., 2019, *ApJ*, **884**, 49
 Tritsis A., Panopoulou G. V., Mouschovias T. C., Tassis K., Pavlidou V., 2015, *MNRAS*, **451**, 4384
 Troland T. H., Goss W. M., Brogan C. L., Crutcher R. M., Roberts D. A., 2016, *The Astrophysical Journal*, **825**, 2
 Vaytet N., Commerçon B., Masson J., González M., Chabrier G., 2018, *A&A*, **615**, A5
 Virtanen P., et al., 2020, *Nature Methods*, **17**, 261
 Whitworth D. J., Smith R. J., Klassen R. S., Mac Low M.-M., Glover S. C. O., Tress R., Pakmor R., Soler J. D., 2023, *MNRAS*, **520**, 89
 Whitworth D. J., et al., 2025, *MNRAS*, **536**, 2936
 Zhao B., Pudritz R. E., Pillsworth R., Robinson H., Wadsley J., 2024, *ApJ*, **974**, 240
 van der Walt S., Colbert S. C., Varoquaux G., 2011, *Computing in Science Engineering*, **13**, 22

APPENDIX A: BAYESIAN ANALYSIS

Bayes' Theorem states that, for a given model, the posterior distribution of the parameters $\theta = (\theta_1, \theta_2, \dots)$ given data D can be written as

$$p(\theta|D) = \frac{p(D|\theta)p(\theta)}{p(D)}, \quad (\text{A1})$$

where $p(D|\theta)$ is the likelihood of D given θ , $p(\theta)$ the prior distribution of the parameters, and $p(D)$ the evidence for data D .

As we are analysing three distinct and different data groups, where the magnetic field strength is derived in different ways, we have to implement different variations of Bayesian analysis. We describe our methods below.

A1 The non-hierarchical Bayesian model

A1.1 Parameters, Likelihood and Posteriors

As a first step, we perform the Bayesian inference with Markov Chain Monte Carlo (MCMC) sampling using the `emcee` code (Foreman-Mackey et al. 2013) on both the observational and numerical data in roughly the same way, with only some variation in the treatment of the errors and in the initial setup of the likelihood based on the model and the prior distributions for the parameters. In this section we present the method we implemented.

As in C10 and following works we assume a broken power-law as our underlying model, which is implemented in the likelihood module of the code. We do not consider the low density regime to be flat but allow its power-law index to vary along with all other parameters. The model y_{mod} for the magnitude of the magnetic field then becomes

$$|\mathbf{B}| = y_{\text{mod}}(\theta) = B_0 \begin{cases} (n/n_0)^{\alpha_1} & \text{if } n \leq n_0, \\ (n/n_0)^{\alpha_2} & \text{if } n > n_0. \end{cases} \quad (\text{A2})$$

Our parameters are thus

$$\theta = (\alpha_1, \alpha_2, n_0, B_0, \ln V), \quad (\text{A3})$$

where n_0 is the number density at which the power-law changes, α_1 and α_2 are the power-law indexes below and above n_0 , B_0 is the magnitude of the magnetic field at n_0 , and $\ln V$ is the nuisance factor to account for intrinsic variance not described by the measurement uncertainties. The nuisance factor is only applied to the errors in B . Assuming that the measurement uncertainties are Gaussian, the likelihood function given a data set $\{y_i\}$ of n points is

$$\ln p(\theta|\{y_i\}) = -\frac{1}{2} \sum_{i=1}^n \left[\left(\frac{y_i - y_{\text{mod}}(\theta)}{s_i} \right)^2 + \ln s_i^2 \right] + \text{constant}, \quad (\text{A4})$$

where θ are the free parameters, y_{mod} is the model as defined in Equation A2 and

$$s_i^2 = \sigma_x^2 + V^2 y_{\text{mod}}^2. \quad (\text{A5})$$

The total variance σ_i in the measurement errors on both the magnetic field and number density, computed from

$$\sigma_i^2 = \sigma_x^2 + \sigma_y^2, \quad (\text{A6})$$

where σ_x^2 is the error propagated from the number density, n , and σ_y^2 is the error propagated from the magnetic field from

$$\sigma_x^2 = \begin{cases} (\alpha_1(B_0/n_0)^{n(\alpha_1-1)} x_{\text{err}})^2 & \text{if } n \leq n_0, \\ (\alpha_2(B_0/n_0)^{n(\alpha_2-1)} x_{\text{err}})^2 & \text{if } n > n_0. \end{cases} \quad (\text{A7})$$

and σ_y^2 is from

$$\sigma_y^2 = y_{\text{err}}^2 + y_{\text{model}} e^{2\log V}, \quad (\text{A8})$$

This is a simple Taylor expansion for error analysis and not fully accurate, but a more detailed study is beyond the scope of this work.

For the Zeeman data we use Equation (A22) described in Appendix A4.

The posterior distribution is proportional to the product

of the likelihood and the prior:

$$p(\alpha_1, \alpha_2, n_0, B_0, \ln V | y, \sigma) \propto p(y, \sigma | \alpha_1, \alpha_2, n_0, B_0, \ln V) \times p(\alpha_1)p(\alpha_2)p(n_0)p(B_0)p(\ln V) \quad (\text{A9})$$

where the priors are assumed to be independent.

A1.2 A study of different priors

[C10](#) tested uniform priors in linear and logarithmic space for all their parameters. We first test independent uniform priors for all parameters θ . We do this as we have little knowledge of how adding in a new free parameter for the diffuse gas will shape the results. Our choice for the range in α_1 goes from -1 to 1. We use the same range for α_2 as we do not know how it will be affected by α_1 . We keep n_0 and B_0 broad but not unphysical and set $\ln V$ to a large range as again we have no prior knowledge on it:

$$\begin{aligned} p(\alpha_1) &= U(-1.0, 1.0) \\ p(\alpha_2) &= U(-1.0, 1.0) \\ p(n_0) &= U(10^{-5}, 10^5) \\ p(B_0) &= U(10^{-5}, 1000) \\ p(\ln V) &= U(-5.0, 5.0), \end{aligned} \quad (\text{A10})$$

where $U(\min, \max)$ is the truncated uniform distribution.

We run the Bayesian analysis for 10^5 steps based on 100 random walkers, remove the first 5×10^4 steps for a burn-in period, and thin to every twentieth result to avoid auto-correlation. We do this on the Zeeman line-of-sight data, taking the errors in n to be a factor of 2 as in the original study (we consider different factors in Appendix [A4](#)), and present the results in Table [A1](#). The errors are large on α_1 and the value for n_0 is high. We note that the distribution of the posterior samples is not well constrained, with large scatter and unclear distributions. We therefore discard this prior for the observational data.

We next test a more constrained flat prior. Our motivation is as follows. By stating a range of -1 to 1 for both α_1 and α_2 , we are assuming that the probability of α_1 lying between, e.g., $-1 \sim -0.8$, is the same as of it lying between $0.8 \sim 1.0$, which is unlikely. Taking into account previous studies that use different data, and knowledge of physically meaningful values of our parameters, we limit each parameter to:

$$\begin{aligned} p(\alpha_1) &= U(-1.0, 1.0) \\ p(\alpha_2) &= U(0.0, 1.0) \\ p(n_0) &= U(10^{-5}, 5 \times 10^3) \\ p(B_0) &= U(10^{-5}, 100) \\ p(\ln V) &= U(-5.0, 5.0). \end{aligned} \quad (\text{A11})$$

We redo the analysis with these new priors on the Zeeman data and get results as presented in Table [A1](#). We run the code in the same way as for the unconstrained priors and find the results to be similar. Looking at the corner plot for the Zeeman data (see Fig. [A1](#)), although the distribution is more constrained, there is a clear bimodality that can be seen in the n_0 - α_2 plot. It is also apparent that both B_0 and n_0 are biased towards low values, likely due to the folded normal distribution used in the likelihood function, see Appendix [A4.4](#).

What this shows is that the prior assumptions have an impact on the posterior distributions, showing that our analysis is sensitive to the choice of prior.

In order to further improve upon our assumptions and better represent the information within the data, we next tested two different Gaussian priors combined with a flat $p(\theta)$. A Gaussian distribution of the form $\mathcal{N}(\mu, \sigma)$, where μ is the mean and σ is the standard deviation, provides higher probability of the parameter value being close to μ , while allowing for a gradual falloff for deviations from this value, unlike the sharp cut-off offered by the uniform distribution. To set up this prior we set α_1 , α_2 and $\ln V$ to the same flat prior used in the previous tests. We do this as we have no real prior knowledge of what values will be, other than the tests performed here. For B_0 and n_0 we choose to use a Gaussian distribution setting μ to the original values reported in [C10](#) and σ to be extremely broad, the standard deviation of the data, so that it can include the broad range of data, giving:

$$\begin{aligned} p(\alpha_1) &= U(-1.0, 1.0) \\ p(\alpha_2) &= U(-1.0, 1.0) \\ p(n_0) &= \mathcal{N}(300, 10^6) \\ p(B_0) &= \mathcal{N}(10, 300) \\ p(\ln V) &= U(-5.0, 5.0), \end{aligned} \quad (\text{A12})$$

We also run a second test where we set $\sigma = 2\mu$:

$$\begin{aligned} p(\alpha_1) &= U(-0.25, 0.75) \\ p(\alpha_2) &= U(-0.0, 1.0) \\ p(n_0) &= \mathcal{N}(300, 600) \\ p(B_0) &= \mathcal{N}(10, 20) \\ p(\ln V) &= U(-5.0, 5.0). \end{aligned} \quad (\text{A13})$$

The results are shown in Table [A1](#) and the right hand plot of Figure [A1](#). In the unconstrained Gaussian prior, B_0 and n_0 are poorly constrained, and both α_1 and α_2 are similar to the unconstrained uniform prior. The truncated Gaussian prior does appear to be better constrained, but care is warranted. By setting the dispersion σ relatively small compared to the range in the data we may well be forcing the fit. The Gaussian effectively becomes a delta function returning its input value. We have tried to mitigate this by not being too restrictive, but we cannot guarantee that we have succeeded without a more detailed analysis, which is beyond the scope of this paper.

Another problem with using a Gaussian prior is that it allows for the code to predict a negative value for the variables, which is physically impossible. This is overcome however in our choice of likelihood function and error treatment discussed in Appendix [A4.4](#), where we implement a folded normal distribution that forces the data to remain positive.

From these tests we find that the truncated uniform prior (Eq. [A11](#)), produces the most reliable fit to the Zeeman line-of-sight data. This is due to the limitations on the Gaussian prior. We use a similar uniform prior set up for the numerical simulations. See Appendix [A2](#) for a detailed discussion of the model used for the DCF data.

However, this is still not a well constrained model. To see if we can improve upon this we next look at a new technique, hierarchical Bayesian analysis.

Prior	α_1	α_2	n_0 (10^3 cm^{-3})	B_0 (μG)
Unconstrained Uniform	$0.28^{+0.14}_{-0.17}$	$0.72^{+0.07}_{-0.09}$	$2.0^{+2.9}_{-1.4}$	$2.1^{+3.9}_{-1.5}$
Truncated Uniform	$0.26^{+0.09}_{-0.18}$	$0.72^{+0.06}_{-0.06}$	$1.8^{+1.1}_{-1.2}$	$1.7^{+2.1}_{-1.2}$
Unconstrained Gaussian	$0.54^{+0.03}_{-0.04}$	$0.49^{+0.24}_{-0.19}$	850^{+820}_{-620}	86^{+110}_{-71}
Truncated Gaussian	$0.16^{+0.11}_{-0.10}$	$0.70^{+0.06}_{-0.05}$	$0.73^{+0.48}_{-0.29}$	$1.2^{+1.1}_{-0.80}$
3D Truncated Uniform	$0.60^{+0.04}_{-0.05}$	$0.46^{+0.06}_{-0.05}$	$4.3^{+5.0}_{-1.5}$	17^{+17}_{-12}
3D Unconstrained Uniform	$0.55^{+0.03}_{-0.03}$	$0.14^{+0.51}_{-0.70}$	8700^{+3000}_{-4600}	800^{+920}_{-570}

Table A1. The median and 68% equal-tailed credible interval for each parameter computed from the posterior samples for the different priors tested on the Zeeman data.

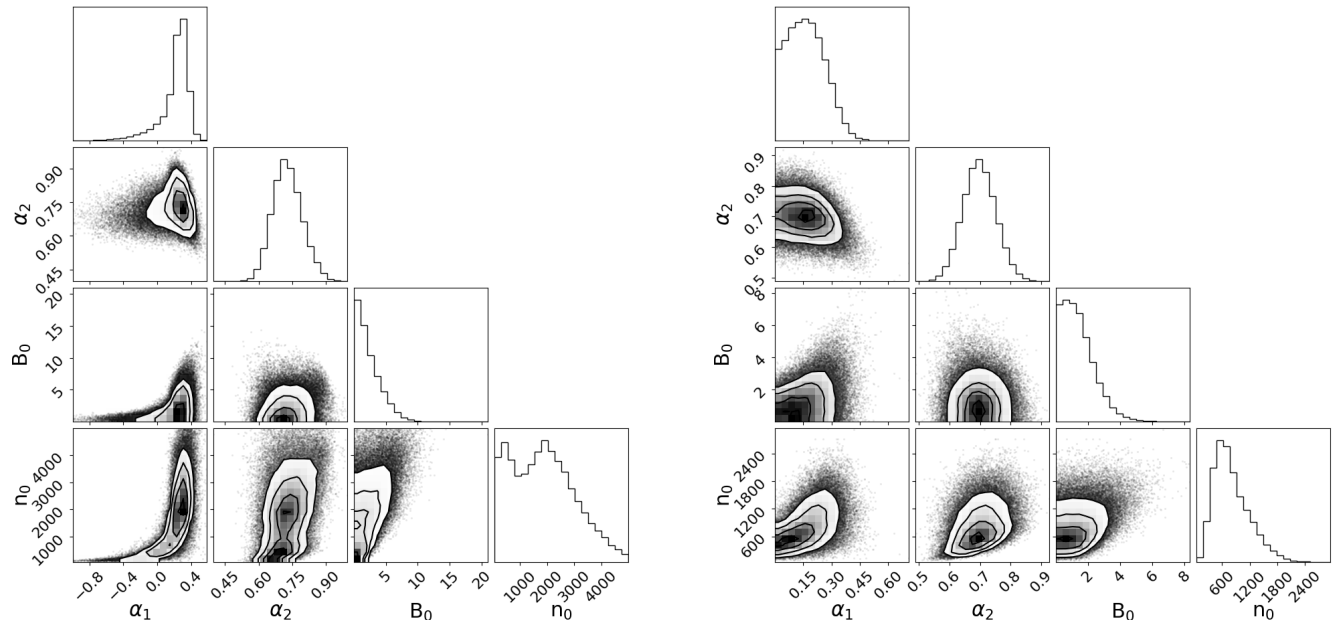


Figure A1. Corner plots for the Zeeman line-of-sight data using the truncated uniform prior (*left*) in Equation (A11) and the truncated Gaussian prior in Equation (A13) (*right*). The distributions for the uniform prior are constrained but show bimodality arising in n_0 suggesting that there could be two break points, though these appear at densities where the Zeeman data is sparse. The truncated Gaussian prior is well constrained and appears to be a good fit, but this is due to the limits placed on the Gaussian function, which constrain the distribution too tightly.

A2 The hierarchical Bayesian model

To overcome the limitations of the previous method, we employ hierarchical Bayesian models. Such models allow us to incorporate a more complete description of how the data are generated. The hierarchical model not only accounts for intrinsic variance in the true values of the density and magnetic field, in addition to the measurement uncertainties, but also incorporates the correlated measurement uncertainties in a straightforward manner. The increase in complexity of the model—more nuisance parameters and more complicated priors for these parameters—results in it being more computationally intensive.

For numerical stability and convergence, we define the model for the base-10 logarithms of the density and field, each scaled by the corresponding minimum data value, $\log_{10} n/n_{\min}$ and $\log_{10} B/B_{\min}$. In the following, we re-

fer to these normalized logarithmic quantities as the density and the field.

The hierarchical models used to represent the DCF and Zeeman data are shown in Figure A2. The models assume that noisy realisations $\tilde{\mu}_x$ of the density are drawn from true values μ_x with intrinsic spread $\sigma_{x,\text{int}}$. True values of the magnetic field are then generated from $\tilde{\mu}_x$ according to the power law

$$\mu_Y = \log_{10} B_0 + \alpha (\tilde{\mu}_x - \log_{10} n_0), \quad (\text{A14})$$

with a change in slope α at some break point (n_0, B_0) .

How the observations are drawn from the $(\tilde{\mu}_x, \mu_Y)$ then differs between the DCF and Zeeman models. The magnetic field strength in the DCF data is directly correlated with number density, (as seen in Eq. 1; see [Pattle et al. 2022](#), for a

detailed discussion), and this should be accounted for in our analysis.

The measurement errors in the Zeeman model are uncorrelated, so each density and field value is drawn independently from their respective true value distributions, with a standard deviation that combines the intrinsic spread and the measurement error at that point in quadrature. The measurement errors in the DCF data, on the other hand, are correlated. Therefore, for each (density, field) pair in the DCF data, we introduce correlation between the density and field measurement errors by defining a covariance matrix

$$\Sigma = \begin{bmatrix} \sigma_{X,\text{int}}^2 + \sigma_{X,\text{meas}}^2 & \rho \sigma_{X,\text{meas}} \sigma_{Y,\text{meas}} \\ \rho \sigma_{X,\text{meas}} \sigma_{Y,\text{meas}} & \sigma_{Y,\text{int}}^2 + \sigma_{Y,\text{meas}}^2 \end{bmatrix} \quad (\text{A15})$$

The observed density and field are then drawn from a multi-normal distribution with mean (μ_X, μ_Y) and covariance matrix Σ .

The hierarchical models were written in the `Stan` statistical modeling language³ using version 1.2.5 of the Python package `CmdStanPy`⁴. Inference is performed using four independent Markov chains with initial values chosen to promote convergence. Each chain is run with 5×10^3 warmup iterations followed by 5×10^3 sampling iterations. The No-U-Turn Sampler algorithm is used, with parameters tuned to maintain an optimal acceptance probability (`adapt_delta = 0.99`) and to prevent excessive tree depth (`max_treedepth = 15`). We confirm convergence of the chains using the Gelman-Rubin (1992) statistic \bar{R} and the bulk and tail effective sample size, all of which are provided as standard outputs by the `CmdStanPy` package's `summary` method. The posterior samples generated by the code are used to construct corner plots and compare the fits to the data, as shown in Figure 1. To evaluate the model's predictive accuracy, simulated datasets drawn from the posterior distributions can also be generated; we show the result of such predictions for the DCF data (bottom right panel in Figure 2).

A3 Inference on the numerical data

An issue in running the Bayesian routine on the numerical simulations is the large number of data points, with each simulation consisting of well over five million points. Running the routine on such large data sets takes substantial resources. To try and mitigate the computational cost, we take five random samples of 10^5 points each from each simulation, using the likelihood function Equation (A4) with priors

$$\begin{aligned} p(\alpha_1) &= U(-1.0, 1.0) \\ p(\alpha_2) &= U(-1.0, 1.0) \\ p(n_0) &= U(0.0, 10^6) \\ p(B_0) &= U(10^{-5}, 1000) \\ p(\ln V) &= U(-5.0, 5.0), \end{aligned} \quad (\text{A16})$$

The initial conditions for the Bayesian analyses are taken from a linear regression fit to the whole data set,

$$(\alpha_1, \alpha_2, B_0, n_0, \ln V) = (0.34, 0.34, 10.0, 300.0, 0.5) \quad (\text{A17})$$

³ <https://mc-stan.org/>

⁴ <https://mc-stan.org/cmdstanpy/>

We take 100 walkers and run 2.5×10^4 steps to ensure convergence. We then combine the five individual data sets for each simulation into one data set, discarding the first 5×10^3 steps and thin to every twentieth data point.

Once the code has been executed, we have five sets of posterior parameter samples for each simulation. We combine these five sets of samples to compute the median and MAP values as well as the corresponding 68% credible intervals for each parameter and present them in Figure 3 and in Appendix A8.

All simulations bar the small and large scale dynamo simulations of Gent et al. (2024) use the same initial conditions as the non-hierarchical Bayesian technique used on the observational data seen in Section A1.1. The reason for the SSD simulations differing is that the data in these diffuse ISM simulations all lie below the values used for the initial condition and so the code does not converge as there is no data to constrain it.

For these four simulations, we instead use:

$$(\alpha_1, \alpha_2, n_0, B_0, \ln V) = (0.0, 0.0, 0.1, 1.0, 0.5) \quad (\text{A18})$$

A4 Observational errors

Before performing inference using the defined likelihood function and priors we need to address the errors on both the observational data and numerical simulations. Bayesian analysis requires error estimates on the observations as they provide the weighting for each data point. We describe the estimation and/or treatment of errors for various observational datasets in this section.

A4.1 Errors on the DCF data

The 700 observations compiled by Pattle et al. (2022) come from numerous different instruments including SCUBA and Planck. This implies substantial heterogeneity in their error treatments. As we do not have the raw data available to re-calculate the errors consistently, we make the approximation that they were all calculated in the same manner. We do the same for the errors in n , assuming they are all calculated in a similar manner.

A4.2 DCF: Symmetrical and asymmetrical errors

Only 319 of the 700 observations have reported errors on magnetic field strength. The data without errors appears mostly at the highest densities, though they do cover the whole density range. Of the 319 that have errors, 26 of them have asymmetric errors and of those, five have a skew of greater than 15%. For number density there are 242 values that have reported errors out of 700. Not all of these data correspond, i.e. data that has errors in n does not necessarily have reported errors in B and vice versa. We select our data set for DCF based on the reported values that have symmetrical errors in B and end up with a data set of 296 data points.

A4.3 DCF: Data lacking errors

For the data that do not report errors we apply symmetric errors using the following method. We first use the data with symmetric errors to estimate the distribution of relative errors using a KDE. We then draw samples from this KDE

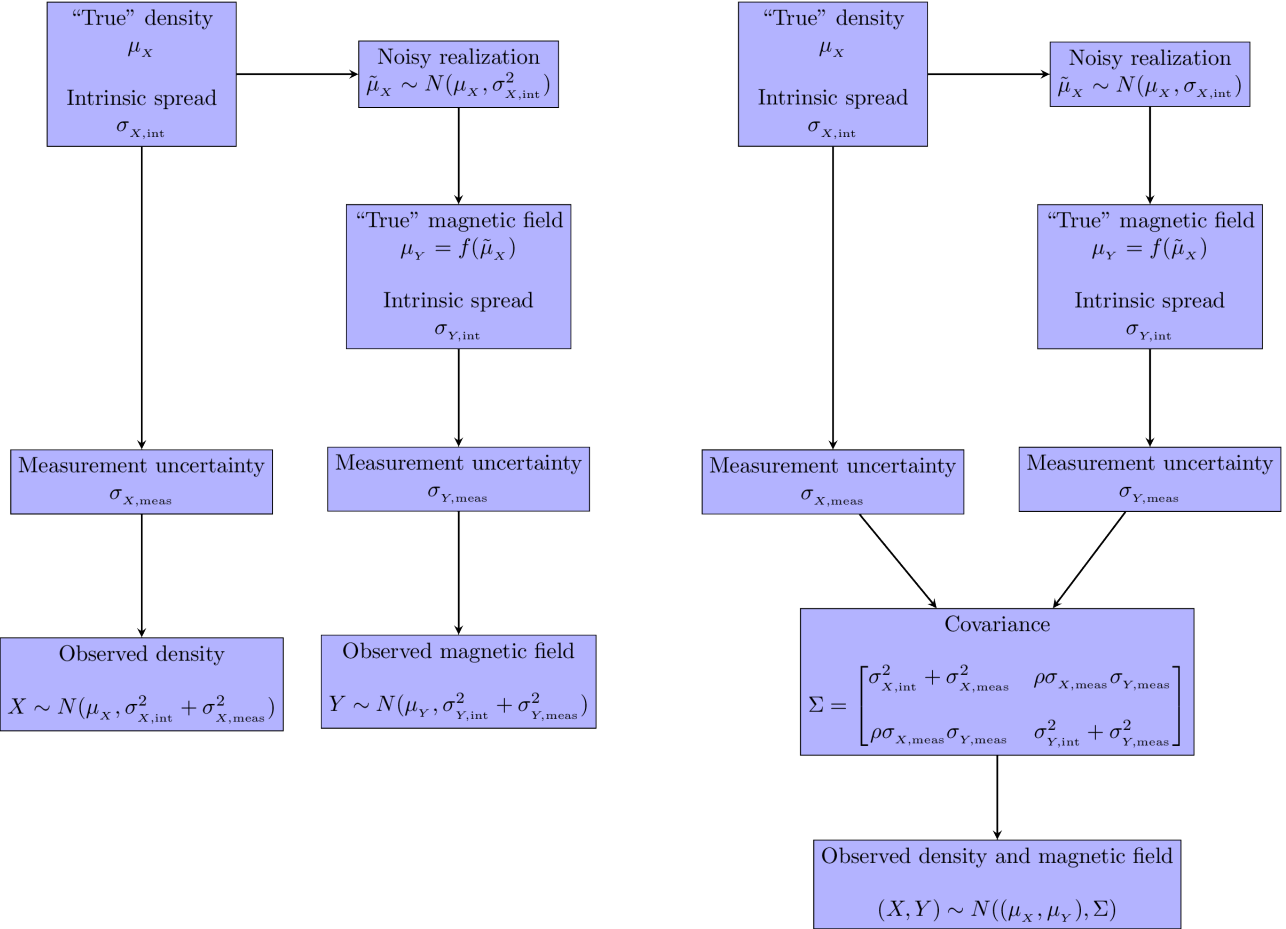


Figure A2. Graphical representation of the hierarchical models used for the Zeeman (*left*) and DCF (*right*) data. See text for details.

and generate error estimates at each point that lacked errors. Thus, each data point has a reported or estimated symmetric error based on observational results. We apply this method for both magnetic field strength and number density data. Figure A3 shows the KDE for the magnetic field strength as an example.

A4.4 Errors on the Zeeman data

The Zeeman data from C10 provides line-of-sight magnetic fields, meaning that we have both positive and negative values of the magnetic-field strength. Whilst this is not an issue for the strength, which can be taken as a magnitude, turning the negative values positive, the treatment of the errors is not as simple. In line-of-sight space the errors are symmetric and can thus be both positive and negative, but when we take the magnitude of the field strength we run into a problem. If the error is larger than the field strength then the error can return negative values of the magnitude of $|B|$, which is not physically possible. To overcome this we split the field magnitude B into line-of-sight and plane of sky components such that

$$B^2 = B_z^2 + (B_x^2 + B_y^2) \equiv B_z^2 + B_{\text{pos}}^2, \quad (\text{A19})$$

where B_z and B_{pos} are the line-of-sight Zeeman and plane-of-sky components respectively. If only one component is mea-

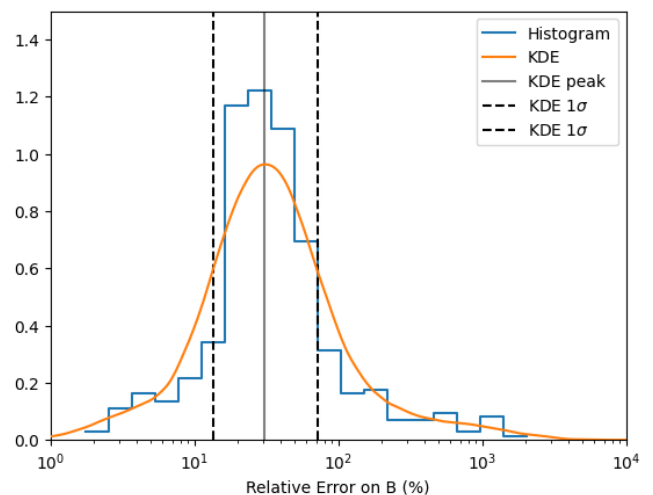


Figure A3. The kernel density estimate (orange line) for the distribution of relative errors, constructed using the symmetric magnetic field strength errors from the DCF data of Pattle et al. (2022). A histogram of the relative errors from the data (blue line) is also shown. The solid vertical line shows the median relative error and the dashed lines show the 1σ spread around it.

sured, B can be estimated by assuming that component is the average value over all possible directions (see Crutcher 2004 and Crutcher et al. 2004 for a detailed discussion on this). Note that because B_z is an odd function, we average over its absolute value. Therefore,

$$B = \frac{4}{\pi} B_{\text{pos}} \quad \text{if } B_{\text{pos}} \text{ measured} \quad (\text{A20})$$

$$B = 2|B_z| \quad \text{if } B_z \text{ measured} \quad (\text{A21})$$

If only B_{pos} is measured, and if the measurement uncertainties are normally distributed, then B is also normally distributed with mean and standard deviation $\pi/4$ times the mean and standard deviation of the B_{pos} measurements⁵. If only B_z is measured with normally-distributed uncertainties, B is then a folded normal distribution. As it is an asymmetric distribution, there is now a non-zero lower bound to the B value for noisy measurements: a measurement $B_z = 0$ produces a non-zero estimate for B due to the finite noise associated with the measurement. Additionally, the asymmetric distribution also implies that the error bars are no longer symmetric. We then have to compute confidence intervals from the underlying distribution.

Assuming that the factor required to convert measurements into the magnitude B is c , the likelihood function for this problem, given a data set $\{y_i\}$ with n points, is then

$$\begin{aligned} \ln p(\theta|\{y_i\}) = & -\sum_{i=1}^n \left[\exp \left\{ -\frac{1}{2} \left(\frac{y_i - y_{\text{mod}}(\theta)}{cs_i} \right)^2 \right\} + \right. \\ & \left. + \exp \left\{ -\frac{1}{2} \left(\frac{y_i + y_{\text{mod}}(\theta)}{cs_i} \right)^2 \right\} + \ln cs_i \right] + \text{constant}, \end{aligned} \quad (\text{A22})$$

where $y_{\text{mod}}(\theta)$ and s_i are defined in Equations (A2) and (A5) respectively. As before, the latter quantity incorporates a nuisance parameter (see Sect. A1.1 for more details) to account for unknown systematic errors and intrinsic variance not explained by the measurement errors.

Setting $c = 2$ in Equation (A22) is equivalent to applying the conversion factor from Crutcher (2004) for Zeeman to three-dimensional field strength. If we set it to $c = 1$ we can compute the probability using the errors on the line-of-sight data. We are also able to use this principle when converting the DCF data from plane-of-sky to three dimensions, using $c = \pi/4$ instead, as described in Crutcher et al. (2004).

For the errors on n we first look to the literature. C10 estimated an error of a factor of two. In follow-up work this has been brought into question as being too constrained and likely subject to variance across the range in density (Tritsis et al. 2015). Jiang et al. (2020) take the error as a free parameter in their study and report in their best model a factor of 9.3. In this work we run three tests for different error approximations using the hierarchical Bayesian method described above. We first take the original factor of two used in C10 as a Gaussian distribution where $1\sigma = 2n$. We also test two other values: a factor of nine based on the work of Jiang et al. (2020), an upper limit and likely over estimation, as

⁵ While this assumption holds for Zeeman data, according to C10, it may not hold for the plane-of-sky data if computed in a manner similar to the DCF data found in Pattle et al. (2022). We can still use the fact that B will have the same distribution as B_{pos} .

Error Factor	α_1	α_2	n_0 ($\times 10^4 \text{ cm}^{-3}$)	B_0 (μG)
2	Median	$0.14^{+0.07}_{-0.09}$	$0.68^{+0.09}_{-0.07}$	$0.34^{+0.55}_{-0.20}$
	MAP	$0.18^{+0.04}_{-0.11}$	$0.67^{+0.08}_{-0.08}$	$0.18^{+0.36}_{-0.13}$
5	Median	$0.15^{+0.06}_{-0.09}$	$0.53^{+0.09}_{-0.07}$	$0.40^{+1.3}_{-0.30}$
	MAP	$0.18^{+0.05}_{-0.10}$	$0.50^{+0.10}_{-0.10}$	$0.26^{+0.53}_{-0.25}$
9	Median	$0.15^{+0.06}_{-0.10}$	$0.46^{+0.08}_{-0.06}$	$0.33^{+1.50}_{-0.26}$
	MAP	$0.18^{+0.05}_{-0.10}$	$0.44^{+0.07}_{-0.06}$	$0.31^{+0.44}_{-0.30}$

Table A2. Median parameter estimates along with 68% equal-tailed intervals calculated from the posterior samples for three different relative error estimates for the number density in the Zeeman line-of-sight data. The mode and the corresponding 68% highest posterior density (HPD) interval are also shown.

well as a factor of five. The results can be seen in Table A2. Whilst we do see some variation in the results when the error factor is changed, the variations are statistically insignificant, all laying within 1σ of each other. For reporting of results we choose a factor 5, this is so we are not constraining them with too small a value or over estimating them with too high a value. However, we do note that having a full and comprehensive understanding off the errors is important for Bayesian analysis but an in-depth analysis is beyond the scope of this work.

One caveat on the method used in this work is that we are assuming all the errors are calculated in the same manner. To treat the errors properly would require each set of observations from a survey or observation to be treated independently with their own nuisance factor. The detail required for that is beyond the scope of this work.

A5 Scaling the B field

Magnetic fields are a three-dimensional vector field and so far we have only considered the observed line-of-sight field strength for the Zeeman observations and the plane-of-sky field strengths for the DCF measurements. There are reported scaling factors for the DCF data (Crutcher 2004):

$$|\mathbf{B}| = \frac{4}{\pi} B_{\text{pos}}, \quad (\text{A23})$$

and for the Zeeman data (Crutcher et al. 2004),

$$|\mathbf{B}| = 2B_z. \quad (\text{A24})$$

however, if we apply these to the data we also need to apply the scaling factor to the errors. This results in just a shift in where B_0 would arise and therefore, do not investigate this.

Pattle et al. (2022) show that the average DCF measurement is a factor $d = 6.3 \pm 1.5$ higher than the average Zeeman measurement. This is a different conversion factor to f already seen in Equation 1 which is applied to the raw data, as d is specifically the ratio between the DCF and Zeeman data. We perform a fit with this discrepancy taken into account where we reduce only the DCF measurements by this factor d . We do not scale the errors as they are likely understated,

Prior	α_1	α_2	n_0 ($\times 10^4$ cm $^{-3}$)	B_0 (μ G)
DCF				
Median	$0.26^{+0.03}_{-0.03}$	$0.63^{+0.12}_{-0.10}$	$1.81^{+3.58}_{-1.29}$	281^{+154}_{-100}
MAP	$0.23^{+0.61}_{-0.01}$	$0.58^{+0.15}_{-0.06}$	$0.81^{+0.81}_{-0.81}$	$1.90^{+1.87}_{-1.87}$

Table A3. The median and 68% credible interval and the MAP with the corresponding 68% HPD interval for each parameter from the posterior samples for the DCF data where the magnetic field strength has been scaled down using the factor of $d = 6.3$ from (Pattle et al. 2022) to match Zeeman magnetic field strengths.

since the DCF over-predicts the field strength. Not reducing the errors also allows for variability in the scale factor.

We run the hierarchical Bayesian analysis on the scaled-down DCF data, with results given in Table A3. The scaling factor applied here is just a ratio between the two data sets and therefore, not well constrained and possibly not representative of the true scaling. Therefore we present this for interest only and note that due to inherent biases these results are also likely to be skewed. We see no statistical variation in the parameters, except in B_0 , which is to be expected as this is the only value to have changed in the data.

A6 Errors on the numerical simulation data

The numerical data from the various simulations do not include error estimates. Whilst there are various methods of applying errors to the data, we choose a simple extension from that used in the observational data. We take the KDE errors calculated from the observational data for both the magnetic field strength and number density in Appendix A4.3 and apply them to the numerical simulations. As with the observational data, we combine a nuisance factor with these measurement errors.

A7 Influential data points

Figure A4 shows two versions of the DCF data set. The right plot is the full data set where we see an outlier at $n > 10^8$ cm $^{-3}$. As previously discussed, the DCF method becomes inaccurate at extremely high number densities. The left plot shows the same data set, but excludes the high density outlier. Table A4 shows that when we exclude the outlier the inferred position of the break changes to a higher density. Due to the uncertain nature of this point we exclude it from our main result.

Our analysis is limited by the fact that the errors in the underlying data sets are mostly broad estimates, with some data completely lacking errors. The lack of errors particularly affects the densest gas ($n > 10^7$ cm $^{-3}$) where Pattle et al. (2022) suggested there could be a turn over and flattening of the relationship. It is also at these densities where the DCF technique becomes difficult and less reliable. This is discussed in more detail in Section 2.1.

The results of an analysis on the full data set is shown in Figure A5, where we have used a KDE to estimate the errors on the 404 DCF data points missing errors (see App. A4 for a detailed description). This figure shows a turn over and reduction at high densities as predicted in Pattle et al.

Data set	α_1	α_2	n_0 ($\times 10^4$ cm $^{-3}$)	B_0 (μ G)
DCF				
Median	$0.26^{+0.01}_{-0.02}$	$0.77^{+0.14}_{-0.15}$	$13.9^{+10.1}_{-7.4}$	463^{+117}_{-104}
MAP	$0.26^{+0.01}_{-0.02}$	$0.78^{+0.15}_{-0.14}$	12^{+8}_{-8}	440^{+130}_{-93}
DCF				
+ outlier				
Median	$0.26^{+0.01}_{-0.02}$	$0.64^{+0.12}_{-0.10}$	$8.80^{+8.70}_{-4.60}$	413^{+121}_{-93}
MAP	$0.26^{+0.01}_{-0.02}$	$0.62^{+0.11}_{-0.10}$	$5.50^{+7.7}_{-3.2}$	370^{+140}_{-62}
DCF_{kde}				
Median	$0.35^{+0.11}_{-0.11}$	$0.04^{+0.05}_{-0.03}$	470^{+350}_{-200}	3600^{+620}_{-590}
MAP	$0.35^{+0.01}_{-0.01}$	$0.01^{+0.01}_{-0.01}$	360^{+300}_{-180}	3600^{+570}_{-630}

Table A4. Median parameter estimates plus their 68% credible intervals and the MAPs for the observational B - n relation for the DCF data set with and without the high density outlier and for the full DCF data that includes the 404 data that are missing errors. The missing errors are calculated using a kernel density estimate. The value of n_0 shifts higher, while the other parameters are relatively unchanged.

(2022). They raise the possibility of an additional transition point. However, that point would occur at densities where the DCF becomes unreliable due to radiation pressure (Lazarian 2020). Unfortunately, these high density points do not have reported errors and are likely to be biasing the result. We therefore do not consider them in our main results.

A8 Tabulated numerical results tables

We provide the results from the numerical simulation data plotted in Figure 3 in tabular form in Tables A5 and A6.

APPENDIX B: HIGH RESOLUTION MHD SIMULATION OF DWARF GALAXIES

To measure the importance of numerical resolution effects, we re-simulated MHD_10 and MHD_SAT from W23 with higher resolution parameters given in Table B1. The new simulations attain resolutions of $r_{\text{cell}} \approx 0.01$ pc at $n \approx 10^6$ cm $^{-3}$ (see Fig. B1). In the diffuse gas, $n \approx 10^{-2}$ –1 cm $^{-3}$, the resolution is below $r_{\text{cell}} < 10$ pc, similar to the resolution of the densest gas in the RAMSES Milky Way-like simulations. The new base gas mass in the cells is set to $1 M_{\odot}$, allowed to vary by a factor of two, and further refined to resolve the Jeans length, which is set to eight cells. The accretion radius around the sink particles is reduced to 0.01 pc. The maximum mass that a sink is allowed to reach is set to $1000 M_{\odot}$, allowing for massive star formation. We have also included the effects of photoionization. The method implemented here is described in Whitworth et al. (2025). The new simulations are run for 10 Myr from the 1 Gyr checkpoint of the original simulations to allow for the new resolution to take effect, a new population of sink particles to have formed, and ensure that no large-scale changes in the behaviour or growth of the magnetic field have arisen (see Fig. B2).

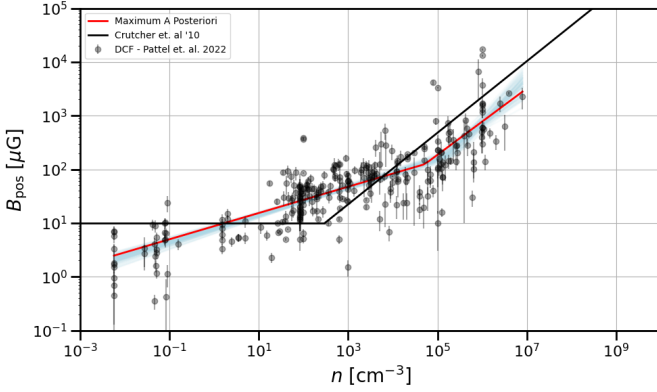


Figure A4. Results from observations of magnetic field strength as a function of number density. Left: The DCF data set from Pattle et al. (2022) with the high density outlier removed. Right: The DCF data set from Pattle et al. (2022) including the high density outlier. The blue lines on these plots are models computed for 100 posterior parameter samples from our analysis. The solid black line on all plots is the relationship proposed by C10.

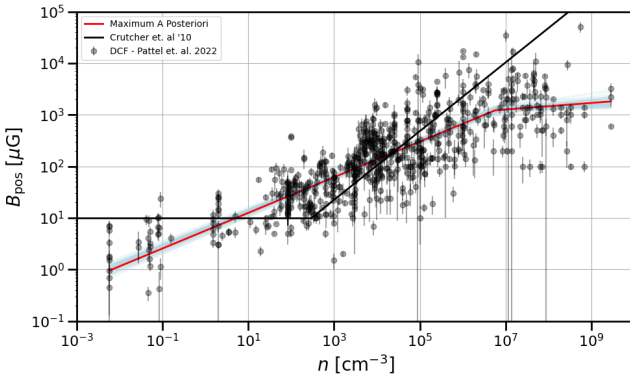


Figure A5. Plot showing the results of the hierarchical Bayesian analysis on the full DCF data set from Pattle et al. (2022) where missing errors have been calculated using a kernel density estimate. We can see here that the relationship does not match the original and has a turn over at the highest densities. These are the densities where it is expected that the DCF method becomes inaccurate due to radiation pressure. We also find that most of the high density points were not reported with errors, introducing uncertainty to the quality of this fit.

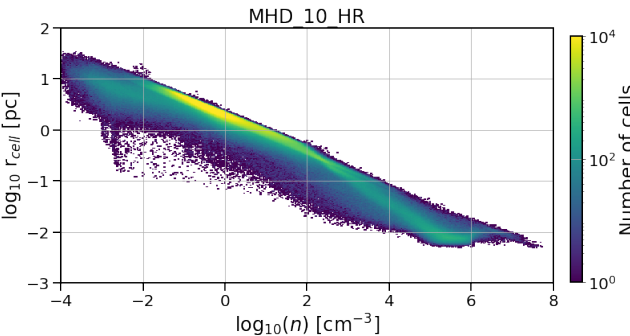


Figure B1. The cell resolution of simulation MHD_10_HR where we can see sub-parsec resolution being reached around number density $n \sim 1 \text{ cm}^{-3}$.

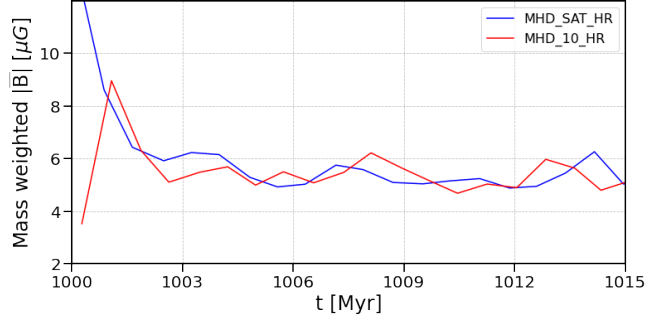
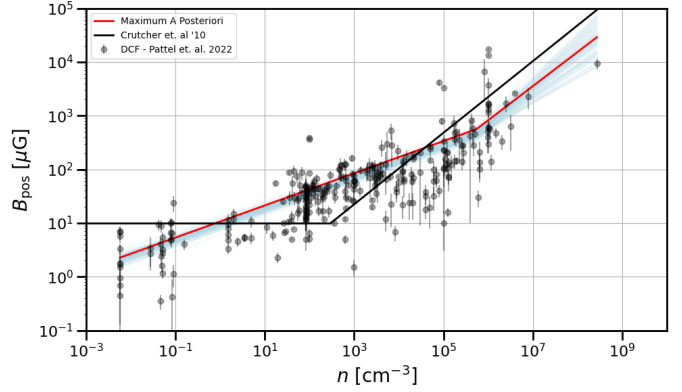


Figure B2. The mass-weighted absolute magnetic field strength in simulations MHD_10_HR and MHD_SAT_HR taken from within a radius of $r = 1.5 \text{ kpc}$ and height $z = \pm 0.2 \text{ pc}$. We see no change in the field strength over the 15 Myr of the new simulations. The peak at the beginning is from the code refining the gas to the new levels.

APPENDIX C: THE DIFFUSE GAS PHASE

We now examine whether the behaviour of the field changes when we better resolve the diffuse gas. We compare the plasma $\beta = P/P_{\text{mag}}$, where $\beta < 1$ means magnetic pressure dominates over thermal pressure, and the Alfvénic Mach number $\mathcal{M}_A = \langle v^2/v_A^2 \rangle^{0.5}$, where if $\mathcal{M}_A < 1$ then the magnetic field dominates the turbulent flow.

Figure C1 shows the difference between the simulations in plasma- β . At high densities magnetic pressure dominates over thermal pressure. At lower densities it is less clear. To be able to see the change we compared the mass fraction of gas with $\beta < 1$ between the simulations. There is no change in the gas mass fraction with $n < 300 \text{ cm}^{-3}$ and $\beta < 1$. However when we look at gas with $n \leq 1 \text{ cm}^{-3}$ the gas mass increases by a factor of 2.9 for MHD_10 and a factor of 0.38 for MHD_SAT.

We now consider the Alfvén Mach number \mathcal{M}_A . Figure C2 shows a comparison between the high resolution and original simulations. Here we can see that in the low density gas the field is slightly more dominant, more so in MHD_SAT_10. But as the bulk of the gas remains at $\mathcal{M}_A > 1$, the overall effect is minimal.

There is a change in the behaviour of the diffuse gas when we better resolve it. This occurs because the field is sup-

Simulation	α_1	α_2	n_0 (cm $^{-3}$)	B_0 (μ G)	Section
NI	$-0.21^{+0.02}_{-0.02}$	$0.56^{+0.01}_{-0.00}$	690^{+11}_{-10}	15^{+0}_{-0}	4.1
IMHD	$-0.27^{+0.01}_{-0.01}$	$0.56^{+0.00}_{-0.00}$	710^{+21}_{-13}	14^{+0}_{-0}	4.1
B3	$0.57^{+0.00}_{-0.00}$	$0.20^{+0.0}_{-0.0}$	$0.45^{+0.01}_{-0.02}$	$1.8^{+0.0}_{-0.0}$	4.2
B6	$0.67^{+0.00}_{-0.01}$	$0.15^{+0.00}_{-0.00}$	$0.26^{+0.01}_{-0.01}$	$2.1^{+0.0}_{-0.0}$	4.2
KPC_LOW	$0.13^{+0.01}_{-0.01}$	$0.36^{+0.01}_{-0.01}$	$1.1^{+0.10}_{-0.10}$	$3.1^{+0.10}_{-0.0}$	4.2
KPC_HIGH	$0.23^{+0.00}_{-0.00}$	$0.13^{+0.01}_{-0.02}$	21^{+4}_{-3}	11^{+0}_{-0}	4.2
SSD_35	$0.30^{+0.0}_{-0.10}$	-1^{+0}_{-0}	$0.16^{+0.23}_{-0.04}$	$0.22^{+0.03}_{-0.02}$	4.2
SSD_98	$0.67^{+0.02}_{-0.01}$	$-0.15^{+0.70}_{-0.01}$	$0.058^{+0.003}_{-0.058}$	$0.29^{+0.01}_{-0.28}$	4.2
SSD_700	$0.69^{+0.00}_{-0.01}$	$0.39^{+0.01}_{-0.01}$	$0.019^{+0.000}_{-0.002}$	$0.50^{+0.0}_{-0.0}$	4.2
LSD_3500	$0.78^{+0.00}_{-0.01}$	$0.012^{+0.002}_{-0.002}$	$0.16^{+0.01}_{-0.00}$	10^{+0}_{-0}	4.2
MHD_10	$0.49^{+0.00}_{-0.00}$	$0.44^{+0.02}_{-0.02}$	360^{+71}_{-110}	11^{+1}_{-2}	4.3.1
MHD_SAT	$0.33^{+0.00}_{-0.00}$	$0.39^{+0.00}_{-0.00}$	10^{+5}_{-3}	$3.4^{+0.50}_{-0.40}$	4.3.1
MHD_10_HR	$0.48^{+0.00}_{-0.01}$	$0.49^{+0.00}_{-0.01}$	700^{+1600}_{-340}	19^{+14}_{-5}	4.3.1
MHD_SAT_HR	$0.28^{+0.00}_{-0.00}$	$0.54^{+0.01}_{-0.03}$	210^{+25}_{-92}	$7.2^{+0.20}_{-0.90}$	4.3.1
MHD_10_LR	$0.84^{+0.03}_{-0.22}$	$0.52^{+0.01}_{-0.19}$	$0.63^{+2900.00}_{-0.07}$	$0.094^{+13.000}_{-0.009}$	4.3.1
MW_RAM_1	$0.56^{+0.00}_{-0.00}$	$0.14^{+0.04}_{-0.03}$	22^{+2}_{-2}	48^{+2}_{-2}	4.3.2
MW_RAM_2	$0.72^{+0.02}_{-0.02}$	$0.46^{+0.00}_{-0.00}$	$0.40^{+0.0}_{-0.10}$	$1.3^{+0.0}_{-0.10}$	4.3.2
MWR_R1	$0.59^{+0.10}_{-0.33}$	$0.52^{+0.01}_{-0.01}$	17^{+6}_{-14}	12^{+2}_{-8}	4.3.2
MWR_R2	$0.61^{+0.01}_{-0.01}$	$0.44^{+0.00}_{-0.00}$	38^{+2}_{-1}	16^{+0}_{-0}	4.3.2

Table A5. The median posterior parameter values in the B - n relation inferred from five sets of random samples from the numerical simulation data, along with the corresponding 68% credible intervals. The last column in every row links to the section where we discuss the corresponding results. In some cases, large relative errors in the inferred parameters arise from outliers due to our random sampling of the data sets. We note the small errors on the exponents α_1 and α_2 showing that they are well constrained for each simulation. It is clear from these results that the relationship changes dramatically across simulations, with large variations in all free parameters.

ported and grown by the turbulent SSD and the LSD. In the diffuse gas the dynamo is poorly resolved if the gas is poorly resolved. The stretch-twist-fold of the field lines that occurs on small, sub-parsec scales then suffers badly from numerical diffusion. [Gent et al. \(2021\)](#) have shown that resolution affects the speed of growth of the field, so in a poorly unresolved diffuse medium the field will grow more slowly than in a well-resolved medium.

Numerical simulations tend not to resolve the diffuse medium for computational efficiency. Galaxy evolution simulations also do not consider the diffuse medium as important as no star formation takes place there. However, the magnetic field in the diffuse medium is dynamically important as it will slow down accretion onto giant molecular clouds, slowing their growth. Sufficiently high numerical resolution is needed to properly simulate these effects (see [Martin-Alvarez et al. 2022](#), for further resolution studies).

One way to determine if the diffuse medium is influenced by the magnetic field is to search for a change to the velocity dispersion σ_v of the gas between dense and diffuse regions. Figure C3 suggests there is little change except at extremely low number densities and $|\bar{B}|$ where the cells are largest and we have likely lost resolution. At number densities where $\mathcal{M}_A > 1$, $n = 10^{-2}$ – 1 cm $^{-3}$, there is little to no change in σ_v between the simulations. Radially there is a slight increase in σ_v in MHD_SAT_HR but not significant enough to make a drastic change. Compared to the strength of the field, we again see little variation.

This paper has been typeset from a $\text{TeX}/\text{L}\text{A}\text{T}\text{E}\text{X}$ file prepared by the author.

Simulation	α_1	α_2	n_0 (cm $^{-3}$)	B_0 (μ G)	Section
NI	$-0.2^{+0.0}_{-0.0}$	$0.56^{+0.00}_{-0.00}$	690^{+10}_{-10}	14^{+1}_{-0}	4.1
IMHD	$-0.27^{+0.01}_{-0.01}$	$0.55^{+0.00}_{-0.00}$	700^{+21}_{-10}	14^{+0}_{-0}	4.1
B3	$0.57^{+0.01}_{-0.00}$	$0.20^{+0.0}_{-0.0}$	$0.45^{+0.01}_{-0.02}$	$1.8^{+0.0}_{-0.0}$	4.2
B6	$0.68^{+0.00}_{-0.01}$	$0.15^{+0.00}_{-0.00}$	$0.23^{+0.04}_{-0.03}$	$2.1^{+0.0}_{-0.0}$	4.2
KPC_LOW	$0.13^{+0.01}_{-0.01}$	$0.36^{+0.01}_{-0.01}$	$1.1^{+0.0}_{-0.10}$	$3.1^{+0.0}_{-0.0}$	4.2
KPC_HIGH	$0.23^{+0.00}_{-0.00}$	$0.13^{+0.02}_{-0.01}$	20^{+4}_{-3}	11^{+0}_{-0}	4.2
SSD_35	$0.30^{+0.0}_{-0.0}$	-1^{+0}_{-0}	$0.16^{+0.00}_{-0.04}$	$0.22^{+0.00}_{-0.02}$	4.2
SSD_98	$0.67^{+0.01}_{-0.01}$	$-0.16^{+0.32}_{-0.03}$	$0.061^{+0.004}_{-0.016}$	$0.29^{+0.01}_{-0.07}$	4.2
SSD_700	$0.69^{+0.01}_{-0.00}$	$0.39^{+0.00}_{-0.01}$	$0.018^{+0.001}_{-0.000}$	$0.50^{+0.0}_{-0.0}$	4.2
LSD_3500	$0.78^{+0.00}_{-0.00}$	$0.012^{+0.001}_{-0.002}$	$0.17^{+0.00}_{-0.00}$	10^{+0}_{-0}	4.2
MHD_10	$0.49^{+0.00}_{-0.00}$	$0.45^{+0.02}_{-0.02}$	390^{+66}_{-100}	12^{+1}_{-2}	4.3.1
MHD_SAT	$0.34^{+0.00}_{-0.01}$	$0.39^{+0.00}_{-0.00}$	$8.1^{+5.1}_{-2.1}$	$3.1^{+0.70}_{-0.20}$	4.3.1
MHD_10_HR	$0.48^{+0.00}_{-0.01}$	$0.49^{+0.01}_{-0.00}$	550^{+580}_{-360}	16^{+8}_{-5}	4.3.1
MHD_SAT_HR	$0.28^{+0.00}_{-0.00}$	$0.55^{+0.01}_{-0.01}$	220^{+26}_{-35}	$7.4^{+0.30}_{-0.40}$	4.3.1
MHD_10_LR	$0.85^{+0.04}_{-0.05}$	$0.52^{+0.02}_{-0.02}$	2^{+1}_{-2}	$0.096^{+0.004}_{-0.016}$	4.3.1
MW_RAM_1	$0.56^{+0.00}_{-0.00}$	$0.14^{+0.04}_{-0.03}$	22^{+2}_{-2}	48^{+2}_{-2}	4.3.2
MW_RAM_2	$0.72^{+0.03}_{-0.00}$	$0.46^{+0.00}_{-0.00}$	$0.43^{+0.01}_{-0.05}$	$1.3^{+0.10}_{-0.0}$	4.3.2
MWR_R1	$0.59^{+0.13}_{-0.02}$	$0.52^{+0.00}_{-0.01}$	15^{+8}_{-1}	12^{+2}_{-1}	4.3.2
MWR_R2	$0.62^{+0.01}_{-0.01}$	$0.44^{+0.00}_{-0.00}$	38^{+2}_{-1}	16^{+0}_{-0}	4.3.2

Table A6. The MAP values in the B - n relation inferred from five sets of random samples from the numerical simulation data, along with the corresponding 68% HPD. The section where we discuss these results is also specified. In some cases, large relative errors in the inferred parameters arise from outliers due to our random sampling of the data sets. We note the small errors on the exponents α_1 and α_2 showing that they are well constrained for each simulation. It is clear from these results that the relationship changes dramatically across simulations, with large variations in all free parameters.

ρ_c (g cm $^{-3}$)	2.4×10^{-19}
n (cm $^{-3}$)	10^5
r_{acc} (pc)	0.01
Softening Length (pc)	0.10
Max sink mass (M_\odot)	1000
Base cell mass (M_\odot)	1

Table B1. Sink particle and resolution parameters used for the new AREPO MHD simulations, with ρ_c the sink density threshold, n the number density of the sink threshold, and r_{acc} the accretion radius. The softening length is the adaptive gravitational softening length of the gas cells and the base cell mass is the target mass of the cell, which is allowed to vary by factor of two.

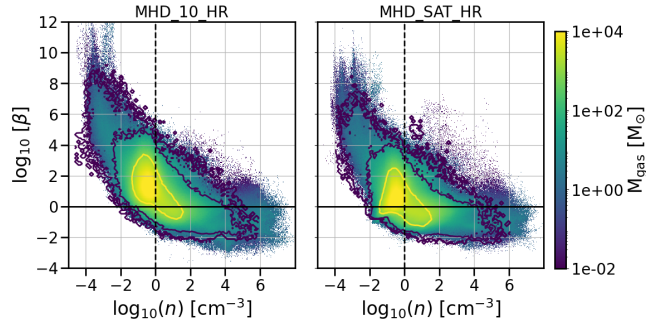


Figure C1. Plasma β versus number density for MHD_10_HR and MHD_SAT_HR. The contours show the same but for simulations MHD_10 and MHD_SAT. The *black horizontal line* shows $\beta = 1$. Below this magnetic pressure dominates over thermal pressure. In the denser regions to the right of the *black vertical dashed line* at $n = 1 \text{ cm}^{-3}$, we see more gas that is magnetically dominated. In the low density gas there is no clear difference.

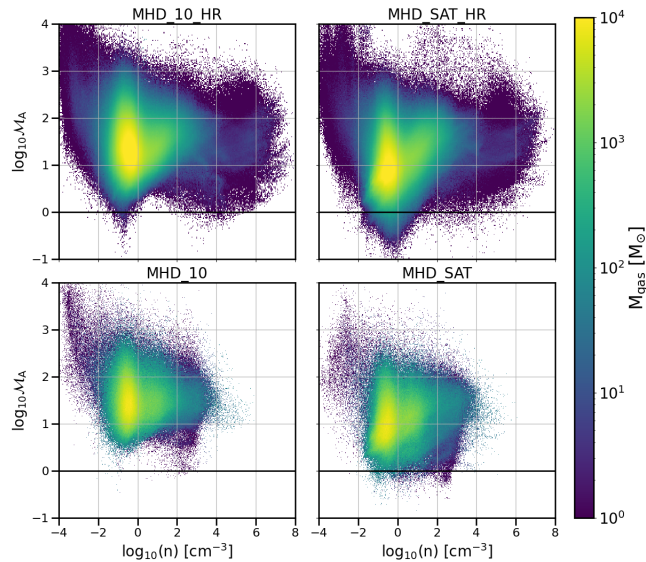


Figure C2. The Alfvénic Mach number \mathcal{M}_A for simulations MHD_10_HR and MHD_SAT_HR (top row) and MHD_10 and MHD_SAT (bottom row). The *black horizontal line* represents $\mathcal{M}_A = 1$. Below this line magnetic pressure dominates and above kinetic turbulence dominates. We can see that in the high resolution simulations, at $n < 1 \text{ cm}^{-3}$ there is more sub-Alfvénic gas with $\mathcal{M}_A < 1$ showing the magnetic field becoming more dominant in that regime.

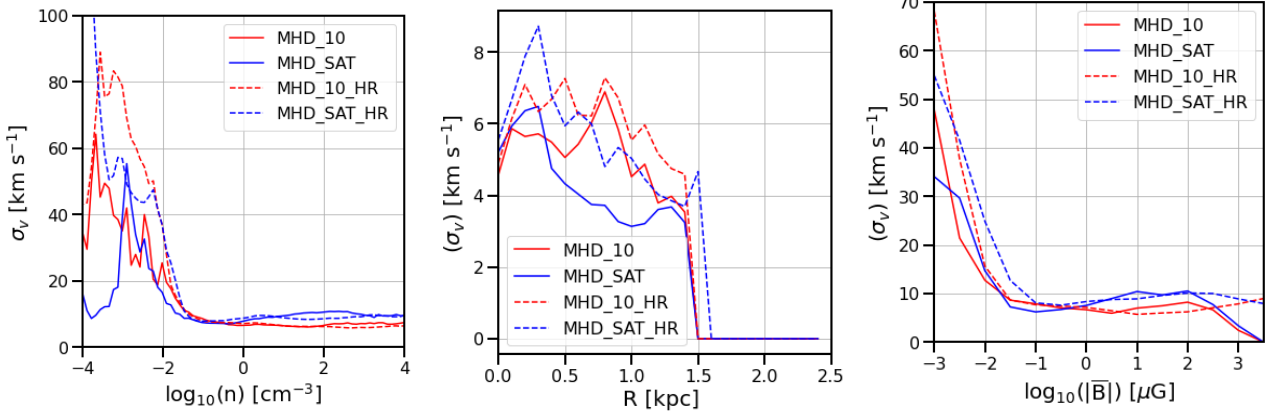


Figure C3. The mass-weighted velocity dispersion σ_v for simulations MHD_10_HR (red dashed), MHD_SAT_HR (blue dashed), MHD_10 (red solid), and MHD_SAT (blue solid). The left panel shows σ_v versus number density n , the middle panel shows the radial distribution and the right shows σ_v versus absolute magnetic field strength $|\bar{B}|$. We can see that in the low field ($|\bar{B}| < 10^{-1}$) and low number density ($n < 10^{-2} \text{ cm}^{-3}$) regime σ_v is much larger. This increase in velocity dispersion is not related to the knee in the C10 relation, but appears at much lower n and $|\bar{B}|$.